Mechanisms for oxygen vacancy defect migration in $SrTiO_3$/NiO heterostructures: Effect of interface layer chemistry and misfit dislocation structure

Anish More, William Ebmeyer, and Pratik P. Dholabhai*

School of Physics and Astronomy
Rochester Institute of Technology
Rochester, NY 14623

* Email: pratik.dholabhai@rit.edu

Abstract

Perovskite-based oxide heterostructures display promising properties resulting from interface phenomena, making them good candidates for next-generation solid oxide fuel cell electrolytes. Among the different features exhibited by these interfaces, misfit dislocations play an important role in influencing ionic transport, yet their role remains poorly understood, a phenomenon also observed in rocksalt-perovskite interfaces. In $SrTiO_3$/NiO heterostructures, we investigate oxygen vacancy migration near misfit dislocations using atomistic simulations in conjunction with high-throughput nudged elastic band-based framework. By comprehensively mapping activation energy barriers across different interfacial chemistries and asymmetric structural features, we explore how the dislocation structure, which is dependent on the local interfacial chemistry, modulates oxygen vacancy migration. This study aims to shed light on the role of dopants, oxygen vacancies, interfacial chemistry, and extended defects in shaping ionic migration at the atomic scale. Misfit dislocations are often considered thermodynamic sinks for oxygen vacancies, oftentimes hindering ionic conductivity at such interfaces. We report dynamic behavior at interfaces that is largely dependent on the local coordination environment, challenging this conventional perspective. The study attempts to bridge the crucial gap in understanding interface-governed ion transport mechanisms in complex oxide heterostructures.

1. Introduction

Complex oxide heterostructures, synthesized through the epitaxial integration of two distinct oxides, constitute an interesting category of materials distinguished by their emergent and often superior physicochemical properties as compared to their individual constituents. These materials have demonstrated transformative potential across a wide spectrum of cutting-edge technologies, including but not limited to Solid Oxide Fuel Cells (SOFCs)[1,2], radiation-resistant nuclear substrates[3], catalytic converters[4], advanced information storage systems[5], and photovoltaic devices[6]. SOFCs, in particular, are a great example of high-efficiency electrochemical converters, capable of directly producing chemical energy from fuel oxidation into electrical power. This makes SOFCs a remarkable candidate to support the transition from carbon-intensive energy sources to sustainable, renewable alternatives.

The interfacial phenomena within these complex oxide heterostructures play a crucial role in altering the properties of the constituent oxides. These junctions inherently facilitate the nucleation of both point and extended defects, which profoundly modulate the material's structural and functional integrity[7]. In lattice-mismatched or semi-coherent heterostructures, the emergence of misfit dislocations at the interfaces serves as an intrinsic mechanism to reduce inter-surface strain resulting from lattice parameter mismatch. These misfit dislocations, which are fundamental structural defects, play an important role in influencing the ionic conductivity and electronic transport characteristics. While their implications for device performance in applications such as SOFCs, next-generation batteries, and heterogeneous catalysis are recognized, the intricate underlying mechanisms by which misfit dislocations dictate interfacial behavior in oxide heterostructures remain poorly understood.

In SOFCs, the solid ceramic oxide electrolyte enables ionic transport from the cathode to the anode. Achieving high ionic conductivity is essential for next-generation SOFCs, which is a basic requirement that drives the research on electrolytes that enable faster ionic diffusion. However, high operating temperatures challenge material stability and durability. Thus, reducing SOFC operating temperatures to the intermediate-temperature (IT-SOFC) range of 773-973 K is necessary for realistic applications. Efforts have been made to reduce the operating temperatures of SOFCs using rare earth metals like Platinum[1,2]. However, the scarcity of rare earth and noble metals, along with other underlying problems, has limited progress in this domain. Thin-film oxide electrolytes, particularly oxide heterostructures, have been shown to offer enhanced efficiency at lower temperatures[8] and are considered promising candidates for IT-SOFCs.

As SOFCs continue to miniaturize, akin to the Silicon Revolution going on in the field of computer architecture, the interface-volume ratio increases, thereby making interface dynamics even more significant. While semi-coherent oxide thin films and heterostructures show superior IT performance, the atomistic mechanisms of ionic transport across interfaces remain debatable. Experimental results on ionic transport across misfit dislocations have yielded varying results, with some reporting enhanced conductivity while others show no appreciable effects[9–11]. On the other hand, computational studies have reported sluggish oxygen diffusion, resulting in diminished ionic transport at homophase dislocations[12,13]. These studies highlight the need for a thorough investigation into the role of misfit dislocations in oxide ion conductivity within thin-film SOFC electrolytes.

Addressing these challenges requires overcoming hurdles encountered in experimental and computational practices. Experimentally, visualizing dopants, interface electrostatic and polarization effects, resolving oxygen vacancy detection issues, figuring out the effects of chemical and structural inhomogeneity remain formidable tasks. On the other hand, theoretical constraints arise due to the minimum system size required to simulate misfit dislocations, limiting Density Functional Theory (DFT) calculations to coherent interfaces, instead of semi-coherent or incoherent interfaces, making the direct study of ionic transport at misfit dislocations infeasible. A practical alternative to DFT is atomistic simulations based on empirical interatomic potentials, which can handle the large system sizes needed to model misfit dislocations in semi-coherent oxide heterostructures, though with some loss of accuracy, at least on the electronic nature of defects.

Depending on the target application, perovskites are often doped to enhance magnetic, ionic, electronic[14], radiative, optical[15], and catalytic[16] properties. Among various oxide materials, $SrTiO_3$ (STO) has been widely studied, with doping strategies employed to tailor its functionality. These materials serve as model systems for investigating ionic transport across oxide interfaces. Rocksalt oxides, such as NiO and MgO, have been of major interest when it comes to SOFCs due to their ability to accommodate oxygen vacancies, which are essential for ionic conductivity in electrolyte and electrode materials[17]. Furthermore, rocksalt and perovskite heterostructures provide a flexible platform for designing complex interfaces with adjustable properties, making them attractive for both SOFC applications and advanced electronic devices. Due to the compositional flexibility of the perovskite lattice (ABO_3), dopants can substitute either A-site, B-site, or O-site ions. Since the present study focuses on oxygen vacancy migration in STO/NiO heterostructures, we limit our discussion to acceptor (p-type)[18] doping, where trivalent dopants like Gd^{3+} replace B-site cations like Ti^{4+}[19]. Acceptor doping strategy facilitates the generation of oxygen vacancies, which facilitates the diffusion of oxide ions in solid oxide electrolytes.

Several doping mechanisms have been reported in the literature, with a multitude of aliovalent dopants employed to modify the properties of perovskites such as STO[20]. However, the dopants bring further challenges since they tend to segregate around the interface regions as opposed to the bulk, often modifying the physical and chemical characteristics[21]. This segregation behavior is influenced by multiple factors such as ionic size mismatch, charge interactions between the dopants and the host atoms, and extrinsic factors like growth parameters and post-deposition annealing treatments[22]. These effects can lead to the formation of space-charge layers that further modify interfacial properties.

For designing fast ion conductors that enable faster ionic diffusion, understanding the influence of dopants is critical, as they alter the oxygen vacancy migration barriers, which ultimately impact ionic transport. Prior studies using DFT[23] and interatomic potential-based simulations[22,24] have demonstrated how dopants influence oxygen vacancy behavior in bulk perovskites. While the effects of acceptor doping in bulk perovskites have been widely explored[20,25,26], much less is known about how these dopants behave in perovskite-based heterostructures, particularly near misfit dislocations. Most prior research has focused on analyzing bulk perovskites[24] and double perovskites[27], with little to no attention paid to the oxygen vacancy diffusion mechanisms at perovskite-rocksalt interfaces. Understanding how trivalent dopants and their associated oxygen vacancies contribute to ionic conduction is critical. To the best of our knowledge, no prior study has systematically investigated oxygen vacancy migration near misfit dislocations in perovskite-rocksalt heterostructures. Given the applications of STO and NiO in SOFC electrolytes and their broader technological relevance, investigating oxygen vacancy transport near dislocations will be beneficial.

Previous studies have characterized oxygen vacancy migration energy barriers in bulk perovskites[24,28], including our recent work on perovskite-perovskite oxide heterostructures[22]. While atomistic simulations based on interatomic potentials have been utilized to study migration energy barriers in the bulk, literature works do not assess the myriad number of pathways possible for oxygen vacancies to migrate throughout the heterostructure, instead choosing to focus on specific transition pathways. Other studies utilizing DFT[29,30] are limited in the number of migration barriers that can be computed due to their high cost. In *Ebmeyer et al*[22], even though we computed the oxygen vacancy migration barriers for the entire structure, the focus was on the interface effects. In contrast, the present work extends that analysis by also investigating oxygen vacancy migration from the interface into the grain interior, thereby offering a more comprehensive view of transport mechanisms in perovskite-rocksalt heterostructures.

In perovskite oxides, defects can often introduce ligand holes, which may in turn alter magnetic properties, as observed in STO. Ligand holes and their impact on properties of rocksalts have also been studied[31–34]. It is likely that the variable oxidation states of dopants can affect the oxygen vacancy formation energies and migration in heterostructures, providing pathways for designing mixed ionic-electronic conductors in SOFCs. However, the present study focuses strictly on defects that form to maintain charge neutrality when trivalent dopants, each with a fixed oxidation state, are substituted into the lattice. Since our goal is to explore qualitative trends in interface-controlled ionic transport, assuming a fixed ionic charge for both dopants and host cations is appropriate. This is justified by the fact that oxygen vacancy diffusion is the dominant mechanism driving ionic conductivity in SOFC electrolytes.

In the present study, we used atomistic simulations to examine the atomic structure of $SrTiO_3$ (STO)/NiO interfaces, as well as to investigate the dislocation network and its impact on oxygen vacancy migration at the heterointerface. In this study, we examine the role of termination chemistry in the formation of misfit dislocation structures. In cases where perovskite oxide heterostructures are implemented as model systems for SOFC electrolytes, knowledge of oxygen vacancy migration pathways in influencing the ionic transport at interfaces would be beneficial. To achieve this goal, we used atomistic simulations in conjunction with high-throughput computing to predict thousands of activation energy barriers for oxygen vacancy migration in STO/NiO heterostructure, with emphasis on misfit dislocations and the interface region. We have studied oxygen vacancy migration pathways at TiO_2–NiO and SrO–NiO interfaces having dissimilar misfit dislocation structures[**Error! Bookmark not defined.**]. The main goal of this work is to offer atomic-scale insights pertaining to the migration behavior of oxygen vacancies near misfit dislocations and shed light on the potential influence of differing misfit dislocation structures on ionic conductivity.

2. Methodology

2.1 Atomistic simulations

Atomistic simulations with 3D periodic boundary conditions (PBC) were conducted within the framework of Large-scale Atomic/Molecular Massively Parallel Simulator (LAMMPS)[35]. The simulations are based on energy minimization using a classical Born-like description of an ionic solid. Parameterized Buckingham[36] pair potentials given by **Equation 1** were utilized to describe the two-body short-range interactions, whereas interactions due to the long-range Coulombic (electrostatic) forces were calculated by means of Ewald's method[37].Owing to the infinitely long threshold for Coulombic interactions, traditional Ewald summation[38], which is a built-in LAMMPS long-range solver, was used, despite the size of the system, to maintain exactness of the solutions.

$$U(r) = Ae^{\left(-\frac{r}{\rho}\right)} - \frac{C}{r^6} + \frac{q_1 q_2}{4\pi\epsilon_0 r}, \qquad (1)$$

where A, ρ, and C are the potential parameters fitted to match the experimental data for a given pair of atoms. The first two terms model Pauli repulsion and van der Waals attraction, respectively, whereas the last term represents the Coulomb potential between ions. These pair potentials are not polarizable, so electric field fluctuations are not allowed within this formalism.

Parameters for the Buckingham pair potential as derived by Busker *et al.*[39], Zacate *et al.*[40], and Minervini *et al.*[41] were used for Sr^{2+}, Ti^{4+}, Ni^{2+}, O^{2-}, and Gd^{3+}. These interatomic potential parameters were chosen since all the divalent, trivalent, and tetravalent cation interactions were fitted against the same $O^{2-} – O^{2-}$ potential[42]. Though the potential parameters used in this work were derived for bulk perovskites and doped lanthanum nickelates, they are expected to qualitatively capture the interface effects for perovskite-rocksalt interfaces. Importantly, the methodology used in this work has been successfully used to study a wide variety of oxide heterostructures[22,43–48] .

Atomic models of STO/NiO heterostructure were constructed for the experimentally observed cube-on-cube orientation relationship, wherein $(001)_{STO}||(001)_{NiO}||$interface and

$[010]_{\mathrm{STO}}||[010]_{\mathrm{NiO}}$. Since lattice parameters are a_{STO} = 3.905 Å and a_{NiO} = 4.16 Å, the lattice mismatch (~6.0%, computed with respect to a NiO substrate) resulting from this orientation relationship is accommodated via the formation of misfit dislocations at the heterointerface. In these atomic models, 15-unit cells of STO were matched with 14-unit cells of NiO to construct a heterostructure with a negligible amount of extrinsic strain. Via cleaving STO at either the neutral SrO or TiO_2 layer and the NiO layer, there are two combinations of heterointerfaces possible, namely SrO–NiO and TiO_2–NiO. For the fully stoichiometric heterostructure, we performed variable-cell energy minimizations under zero external pressure using both conjugate gradient and steepest descent algorithms. Volume was allowed to change, wherein the simulation box was allowed to relax along all directions to eliminate internal stresses and obtain a fully relaxed structure. To achieve globally energy-minimized configurations, 0 K relaxed structures were further annealed using the Nosé-Hoover thermostat, by heating them to 1000 K and allowing them to slowly cool to 0 K over a duration of 10 ns.

A wide variety of trivalent dopants can be added to improve the properties of perovskites, as they have a net effective charge that affects the electroneutrality condition, and thereby the defect equilibria[21,25,26,43,49]. In perovskites, trivalent dopants can replace either of the cations on the *A* and *B* sublattices. For instance, in STO, replacing Ti^{4+} with trivalent dopants leads to acceptor doping (*p*-type)[18]. The defect reaction governing the addition of trivalent dopants to TiO_2 (STO) can be expressed in Kröger–Vink notation as:

$$M_2O_3 \xrightarrow{BO_2} 2M_B' + V_O^{\cdot\cdot} + 3O_O^{\times}, \qquad (2)$$

where $V_O^{\cdot\cdot}$, B, and M correspond to the oxygen vacancy, B-site cations (Ti^{4+}) and trivalent dopants (Gd^{3+}), respectively. Owing to ionic compensation, this reaction indicates that the substitution of two B-site cations with trivalent dopants will result in the formation of one oxygen vacancy. The formation and migration of oxygen vacancy is at the heart of our work [50,51], so we will strictly focus on its migration at disparate interfaces and in the vicinity of Gd^{3+} dopants for diverse nearest neighbor scenarios. In p-type oxides used for catalysis, surface oxygen vacancies become doubly positively charged, which lowers their formation energy and results in a higher defect concentration[50,51]. In addition, researchers report that space-charge regions impact the concentration of oxygen vacancies at oxide surfaces. The type of vacancy reported[51] is consistent with the current work. However, studying the fundamental impact of space-charge regions at such complex interfaces is beyond the scope of this work since we study dilute doping fractions that result in dilute oxygen vacancy concentration. Furthermore, we study the role of oxygen vacancies in the neighborhood of trivalent dopants, which is not the case in the study by Richter *et al.*,[51] since it neglects the role of dopant-defect clusters.

It is anticipated that DFT calculations would offer a better description of migration pathways by including electronic effects. However, these calculations are beyond the scope of this work primarily due to computational time and system size, both of which enter the realm of the impossible when it comes to employing DFT since the supercell size in this work is ~5.76 × 5.76 × 6.66 nm^3 (21,544 atoms). Furthermore, we recently computed the electronic structure and predicted the atomic-scale structure of misfit dislocations at CeO_2/MgO heterostructures using DFT[52] and compared it with atomistic simulations[53]. We found that the atomic structure and qualitative trends for dopant-defect cluster stability predicted using DFT and atomistic simulations agree very well. This agreement not only validates the current approach but also reveals that the underlying assumptions of the method remain truthful.

A usual critique of the methodology based on interatomic potentials is that they are unsuitable for complex chemical environments for which they are not fitted, such as interfaces and transition states for migration barrier calculations. To address this, we validated the potential parameters used in this work by applying them to bulk reference structures and verifying that the resulting relaxed atomic configurations retained ideal bond lengths and unit cell dimensions. Agreement with expected structural metrics affirmed the suitability of these parameters. Furthermore, we have successfully employed this methodology to investigate the thermodynamics and kinetics of defects at interfaces[7,43–45,48,53–55], surfaces[53,56], steps[46,57], and grain boundaries[58–60] in complex oxides. In addition, we have effectively used this methodology to study structure-property relationships at misfit dislocations, as well as compute migration barriers in an intricate chemical environment[45]. Crucially, we have used classical force fields to interpret the experimental observations by predicting qualitative structure-property trends and basic mechanisms at oxide interfaces, which include perovskites.

2.2 High-throughput framework development

A typical oxide heterostructure contains tens of thousands of distinct oxygen migration pathways. To systematically compute these activation energy barriers, we developed a high-throughput framework, OMEGA (Oxygen Migration Energy Graph Algorithm), integrating classical NEB calculations within a Python- and LAMMPS-based workflow. The Nudged Elastic Band (NEB)[61–63] method was used to model vacancy migration to nearest neighbor oxygen sites, and the resulting barriers were mapped across the structure. OMEGA also automates structure generation, dopant placement, and barrier mapping for a wide range of configurations. A schematic of the framework is shown in **Supporting Information (SI) Figure 2**.

3. Results & Discussion

3.1 Atomic scale structure of the interface

There have been studies explaining the growth mechanisms for rocksalt crystals on top of STO[64–66]. The results clearly show that for cube-on-cube developed rocksalt on top of perovskite oxide heterostructures, two different types of interfaces are recognizable. Atomic models of STO/NiO interfaces were constructed based on these experimental observations. For cube-on-cube orientation relationship, depending on the interface layer chemistries involved in the formation of the interface, two different SrO-NiO and TiO_2-NiO interfaces were constructed, which are depicted in **Figure 1**. The heterostructures were energetically minimized and further annealed to predict an energetically and geometrically stable structure. Our approach is validated by the work of *Takahashi et al* [64] which explains how the STO cleaved planes along the $\langle 100 \rangle$ direction alternate between SrO and TiO_2 and the singular NiO neutral $\langle 100 \rangle$ plane results in the formation of two distinct interfaces. Shown along the interface normal direction, **Figure 1a** and **Figure 1b** depict the minimized and subsequently annealed configurations of SrO-NiO and TiO_2-NiO interfaces, wherein only the termination layers from either side of the heterointerface are shown. The interfaces in **Figure 1** have been expanded in the x and y direction ($2 \times 2 \times 1$) to clearly demonstrate the stackings arising due to the misfit dislocations. Our visualization enables us to predict that the SrO-NiO interface has a dislocation structure with a Burgers vector of $\vec{b} = \langle 100 \rangle$, whereas TiO_2-NiO interface has a dislocation structure with burgers vector of $\vec{b} = \langle 110 \rangle$, which agrees well with our reported predictions for the STO-MgO heterostructure[44,48]. We further confirmed the misfit dislocation structure with our in-house maximal bond displacement and interface energy profile analysis scripts (**SI Figure 1**). While experimental studies have demonstrated the formation of rocksalt crystals on perovskite oxide substrates with cube-on-cube epitaxy[67], the influence of interface layer chemistry on the resulting misfit dislocation structures remains poorly understood. Given that these dislocation structures are expected to vary with interfacial composition, and in turn significantly affect interface-dominated properties[43,44], it is crucial to investigate the fundamental mechanisms dictating the behavior of defects at oxide interfaces.

Figure 1. *Minimized and subsequently annealed STO/NiO interfaces. (a) SrO–NiO interface (b) SrO–TiO2 interface. The view is normal to the interface plane. In (a) and (b), STO layer is shown on top. Coherent stackings are highlighted for clarity, and they repeat perpetually along the respective burgers vector directions. Black lines indicate the misfit dislocation network. Atomic colors are given below the panels. Oxygen ions in STO and NiO are colored differently for clarity. The original supercell has been expanded along the [100] and [010] direction to give a 2×2×1 interfacial structure.*

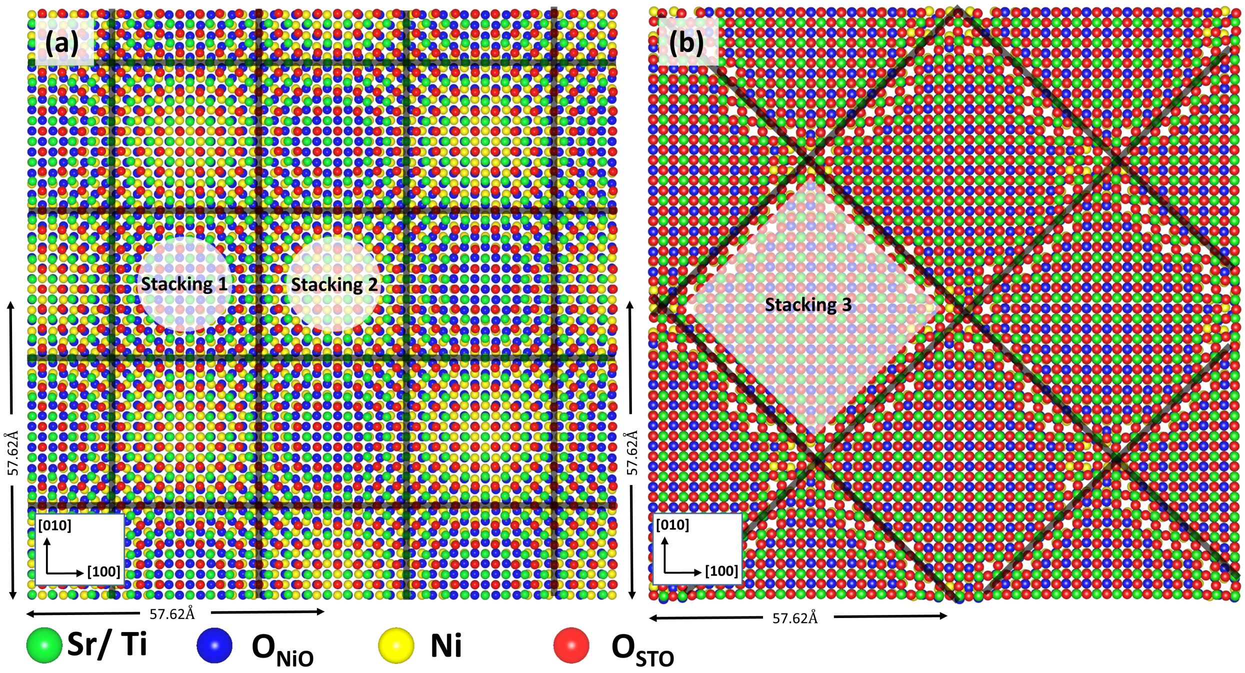

Analysis of atomic configurations at both the interfaces highlights three distinct coherent stackings or zones, which are highlighted in **Figure 1**. As mentioned earlier, a wide array of tools was utilized to distinguish and confirm the location and direction of coherent stackings, including visualization tools, interfacial energy profile analysis (**SI Figure 1**), and maximally displaced bond length analysis. In the SrO-NiO interface, coherent stackings were found within one to less than one lattice constant of the distorted regions. We have labeled the oxygen atoms in the STO layers as O_{STO} (red) and those in the NiO layers as O_{NiO} (blue). Based on the notation developed in our previous work, we will denote the atomic pairs across the interface by the {/} notation. For example, {Ni/O_{STO}} represents a coordination (pairing) between the Ni atom from the NiO interface and the oxygen atom from the STO interface. Similarly, [ ] will indicate the absence of any coordinating atom (nearest neighbor bonding species) for that particular atomic species across the interface. **Figure 2** highlights the cross-interface coordination pairs for the three stackings identified in **Figure 1**.

The coordinating atom environments for the two interfaces can be broadly categorized as follows: (i) SrO-NiO interface: (a) Stacking 1: {O_{STO}/Ni}, {Sr/Ni}, and [O_{NiO}]. (b) Stacking 2: {Sr/O_{NiO}}, {O_{STO} /O_{NiO}}, and [Ni]. (ii) TiO_2-NiO interface: (a) Stacking 3: {Ti/O_{NiO}}, {O_{STO}/Ni}, and [O_{NiO}]. It is evident from these coordination environments for different stackings that at the SrO-NiO interface, even though both the stackings show repulsive interactions, they arise from different electrostatic regimes. A cation-cation repulsion emerges for Stacking 1 and an anion-anion repulsion for Stacking 2. The interfacial coordination pairing is further complicated by the presence of additional coordination pairs, dissimilar chemical bonding, and energy, which yields different configurations for both the coherent stackings in the SrO-NiO interface. The region in between these two distinct stackings is composed of misfit dislocation lines and intersections. On the other hand, at the TiO_2-NiO interface, we have favorable electrostatic interactions due to the {Ti/O_{NiO}} and {O_{STO}/Ni} coordination pairs. At the same interface, the electrostatic behavior at the misfit dislocation intersections will be governed by the isolated oxygen atoms from either side of the interface arranged alternately along the misfit dislocation lines. The coordination pairs for oxygen atoms in the misfit dislocation region are denoted by {O_{STO}/Ni}, {Ti/O_{NiO}}, [O_{NiO}], and [O_{STO}]. Repulsive interactions lead to differences in interfacial chemistry, which is favorable for defect formation[44,46]. **Figure 3a** and **Figure 3b** display the side view of the interface regions for TiO_2-NiO and SrO-NiO interfaces, respectively. In both cases, misfit dislocations are marked by the mismatch of the cation-cation pairing at the interface, almost at the center of the heterostructures. This arises due to the varying cation-anion ratios in both the interface regions. It is important to note that the actual thickness of the film studied is ~6.66 nm, but for clarity, these figures only highlight two unit-cell-thick regions on either side of the interface.

Figure 2. *Coordination pair environments across the interface for the three stackings introduced in **Figure 1**. Panels (a), (b), and (c) show, from left to right: a top-down atomic visualization of each stacking, a side view of the highlighted atomic rows isolated from the structure, and the corresponding cross-interface coordination pairs on the right.*

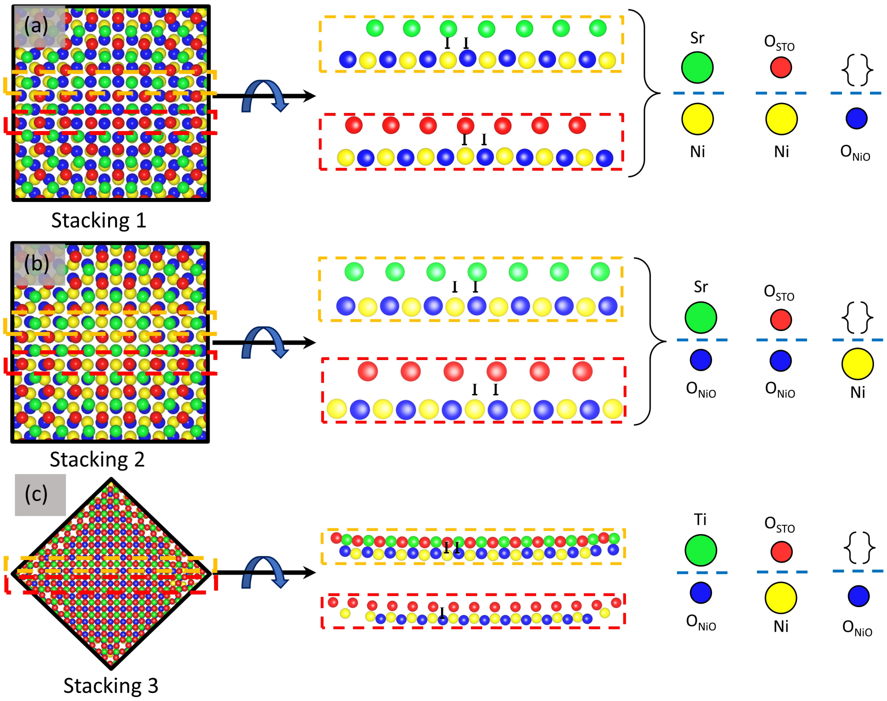

3.2 Defect migration at oxide interfaces

Since one of the primary mechanisms responsible for ionic transport in SOFC electrolytes is oxygen vacancy migration, it is imperative to study disparate vacancy migration pathways as they diffuse throughout the material. We use STO/NiO as a model system to study oxygen vacancy migration at the interfaces as well as throughout the entire structure with the goal of understanding how misfit dislocations affect the migration of oxygen vacancies. To this end, we developed a high-throughput framework to compute the hundreds of thousands of nearest neighbor activation energies for oxygen vacancy migration within the STO/NiO heterostructure.

Figure 3. *Side view of the energetically minimized and annealed STO/NiO heterostructure for (a) TiO_2-NiO interface and (b) SrO-NiO interface. Atomic color scheme is given below the figure.*

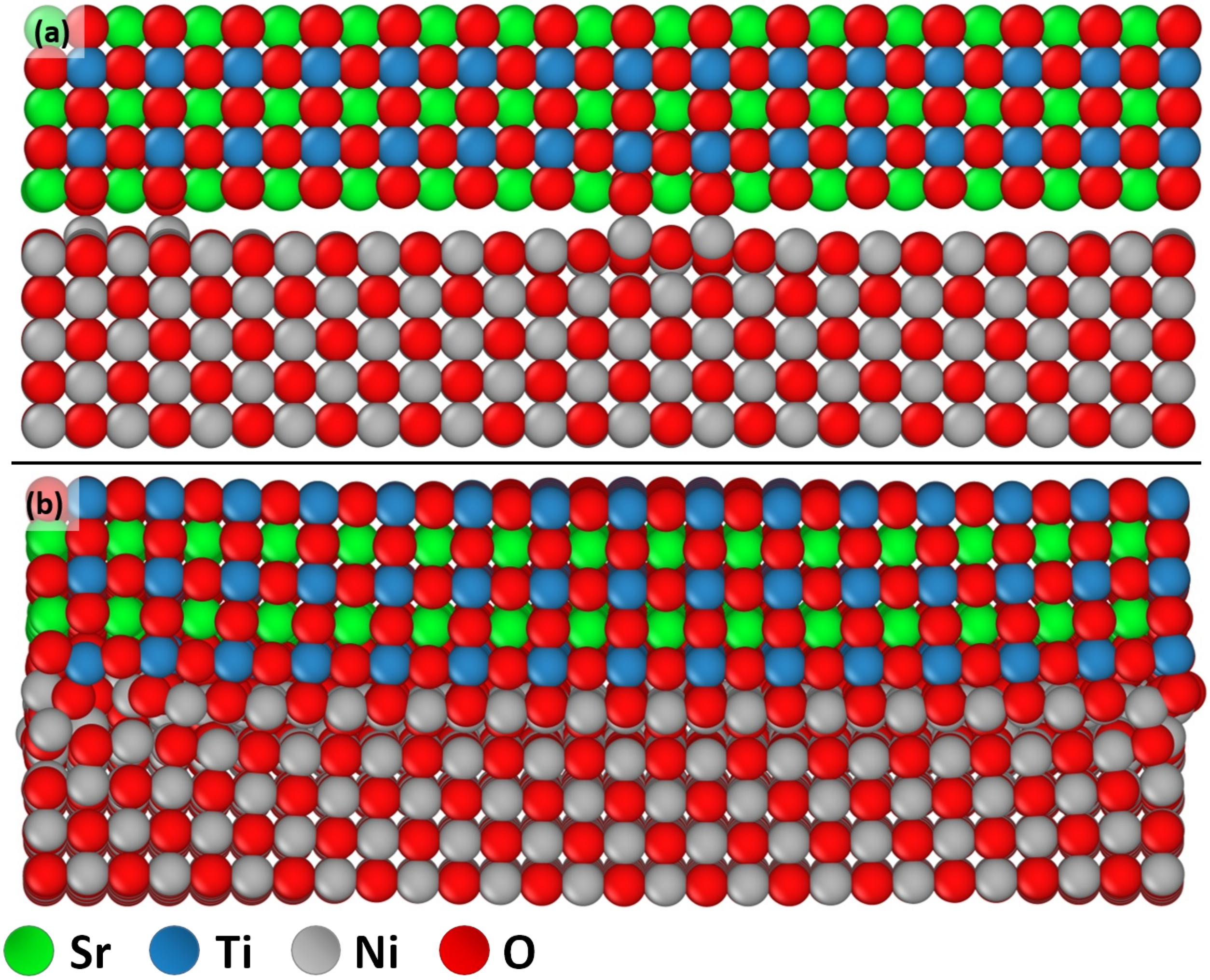

As mentioned earlier, in this work, we strictly focus on doping the B-site cations of the perovskite lattice (TiO_2 layer), which will result in the formation of oxygen vacancies on the oxygen sublattice. We systematically considered all the layers in the heterostructures. In addition to studying the oxygen vacancy migration mechanisms within one particular interface layer, we also studied intra-layer hops. Moreover, for all the layers, we studied four different configurations for placing 10 dopants and the resulting 5 vacancies. For the TiO_2 layer, three of these configurations were chosen with dopants placed as nearest neighbors, whereas in the fourth configuration, dopants were isolated. For all the other layers, we studied four different randomized dopant configurations. In all cases, the doping limit is rather dilute considering the system size is

21,544 atoms. However, to examine the interface effects, we placed all the dopants at the interface layer, which resulted in a dopant fraction of ~4.4% at the interface layer. While this concentration is still dilute in comparison to experimental values, it offers reasonable comparison with realistic scenarios. For each of the interface configurations, ~1400-1700 nearest neighbor migration energy barriers were computed for a single side of the interface. In addition, we computed ~100,000 migration energy barriers for the entire structure. In total, ~1,000,000 migration energy barriers were computed to obtain a thorough understanding of the oxygen vacancy migration landscape near misfit dislocations.

Given in **Figure 4a** are 12 possible nearest neighbor jump directions for the oxygen vacancy starting from the NiO layer. **Figure 4b** shows a top-down view of the NiO layer, which depicts the 4 nearest neighbor pathways for in-layer migration of an oxygen vacancy. In addition to the migration pathways depicted in **Figure 4b,** we have also studied the migration pathways for an oxygen vacancy located in the NiO layer at the interface migrating towards the bulk NiO layers. Since we are interested in studying the NiO layer migration pathways, data showing activation energy barriers for oxygen vacancy migration will be shown for the network consisting of 4 inter-layer pathways, given in **Figure 4b,** along with data showing the same for the network consisting of 4 intra-layer pathways. Similar possible nearest neighbor jump directions for oxygen vacancy situated in the TiO_2 layer are shown in **Figure 4c,** while the corresponding top-down view of the in-layer migration pathways for the vacancy are highlighted in **Figure 4d**. Owing to larger inter-atomic distances between oxygen atoms in the SrO layer as compared to the inter-atomic distances between oxygen atoms in the SrO layer and those in the TiO_2 layer, the only possible nearest neighbor jump directions for an oxygen vacancy in the SrO layer are out of the layer, which are shown in **Figure 4e**. It is important to note that though migration energy barriers were computed for vacancy migration throughout the supercell, we limit the discussion to the interface region. This strategy allows us to establish a correlation between defect migration and the asymmetric interface atomic-scale structure, as well as the disparate coordination environments at misfit dislocations.

Figure 4. *(a) Possible 12 nearest neighbor jump directions for an oxygen vacancy in the NiO layer are shown. (b) Normal view for the NiO layer depicting the 4 nearest neighbor in-layer jump directions. The 4 in-layer direction and other intra-layer directions will be used in following figures to show the magnitude of activation energy barriers on the NiO interface layers. (c)*

Possible 8 nearest neighbor intra-layer jump directions for an oxygen vacancy in the TiO_2 layer are shown. (d) Normal view for the TiO_2 layer depicting the 4 nearest neighbor in-layer jump directions, (e) Possible 8 nearest neighbor intra-layer for an oxygen vacancy in the SrO layer are shown. There is no possible in-layer jump direction in the SrO layer. The intra-layer jump directions will be used in the following figures to show the magnitude of activation barriers on the SrO interface layers. Atomic color scheme is given below the figure.

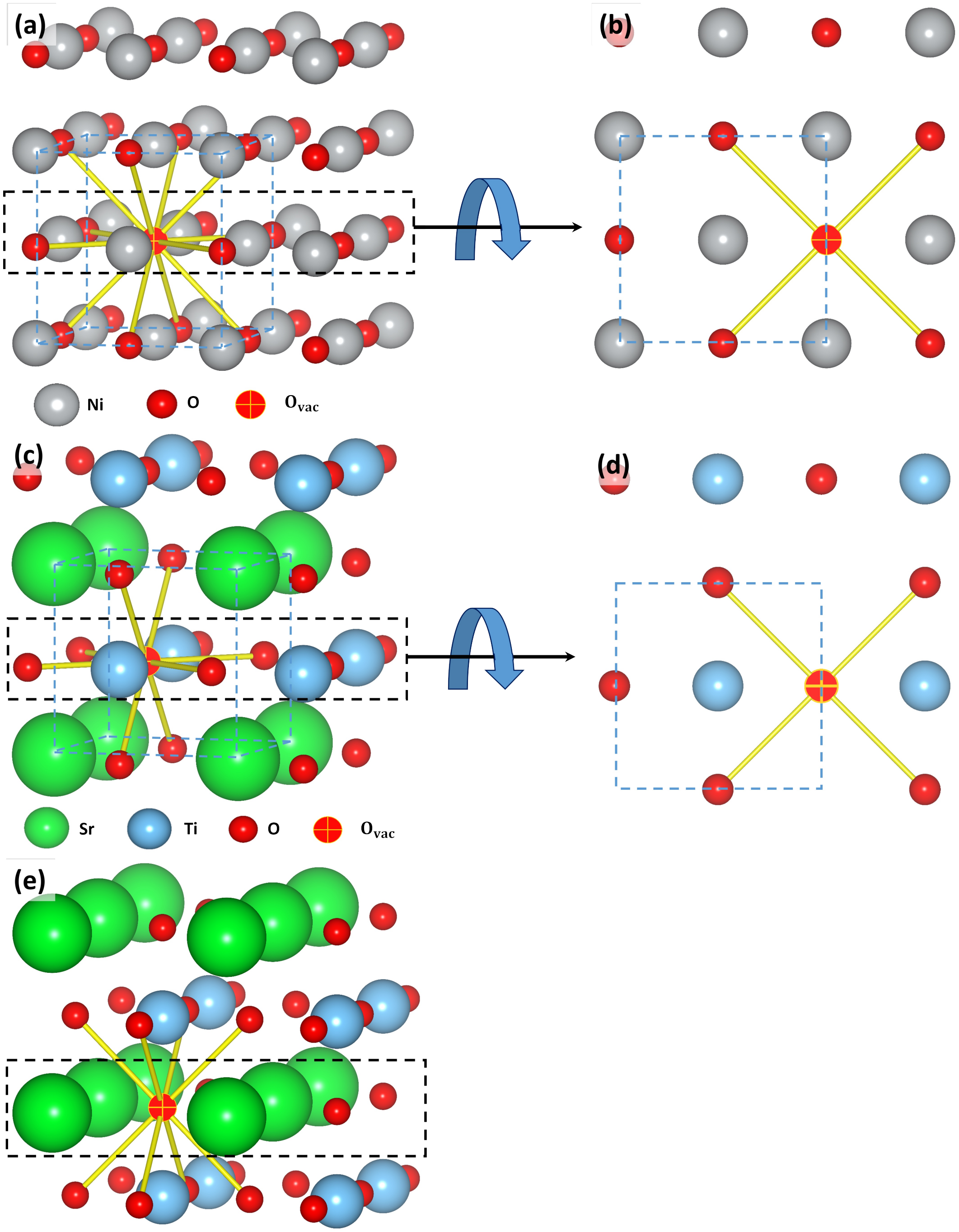

Figure 5- Figure 10 display the activation energies for nearest neighbor oxygen vacancy migration jumps in the vicinity of different dopant distributions at TiO_2 side of TiO_2–NiO, SrO side of SrO-NiO, NiO side of TiO_2–NiO, and NiO side of SrO–NiO interfaces, respectively. **Figure 7** and **Figure 9** display the activation energies for the NiO side of the TiO_2–NiO and SrO–NiO interfaces, respectively, but for the intra-layer migrations as opposed to the in-layer migrations shown in **Figure 8** and **Figure 10**. The color coding for the atoms is indicated in the legends beneath **Figure 5- Figure 10**. We limit the simulations to computing the migration barriers for the first nearest neighbor jumps, which are displayed in all the figures. In **Figure 5**, panels **b, c,** and **d** represent cases where gadolinium dopants are placed in nearest neighbor pairs, which are randomized, whereas in panel **a**, the dopants are isolated. In **Figure 6- Figure 10**, all the panels display randomized dopant configurations. Preparing starting samples with nearest neighbor dopants and oxygen vacancies is reasonable since we have shown that dopant segregation is likely to occur where dopants are next to the oxygen vacancy, that is, in clusters at misfit dislocations in complex oxide heterostructures[54]. The direction of the arrows indicates the jump direction, and their colors indicate the corresponding migration energy barrier associated with the jump. In **Figure 5- Figure 10**, the jumps are shown in the interface normal direction so that the atomic scale structure can be overlaid and compared with that given in **Figure 1**, wherein the supercell is extended in the *x* and *y* direction.

The activation energies near the misfit dislocations show varying characteristics depending on the different interface layers, which is expected because interface defects have been reported to influence migration energy barriers from DFT calculations for perovskite surfaces[68] and atomistic simulations of perovskite-perovskite interfaces[55]. Our current approach is justified as activation energies for oxygen vacancy migration in bulk STO and bulk NiO were found to be 1.4 eV and 1.2 eV, respectively, which agree well with the reported DFT[69], atomistic simulations[70], and experimental values[71]. The aforementioned methodology has also proven to be a good statistic to study transport mechanisms in perovskites[72].

Figure 5. *Activation energy barriers for in-layer oxygen vacancy defect migrations at the* TiO_2*-terminated layer of the* TiO_2*-NiO interface. In (a), each* Gd^{3+} *dopant ion is isolated; in (b), (c), and (d), two* Gd^{3+} *dopants are placed next to the oxygen vacancy in different configurations. The vacancy starting position is indicated with a dashed circle and misfit dislocations are indicated by*

dashed lines. For ***Figure 5-Figure 10,*** *view is normal to the interface, same as in* ***Figure 1****, and atomic color scheme is given below the figure and energy scale is given on the right.*

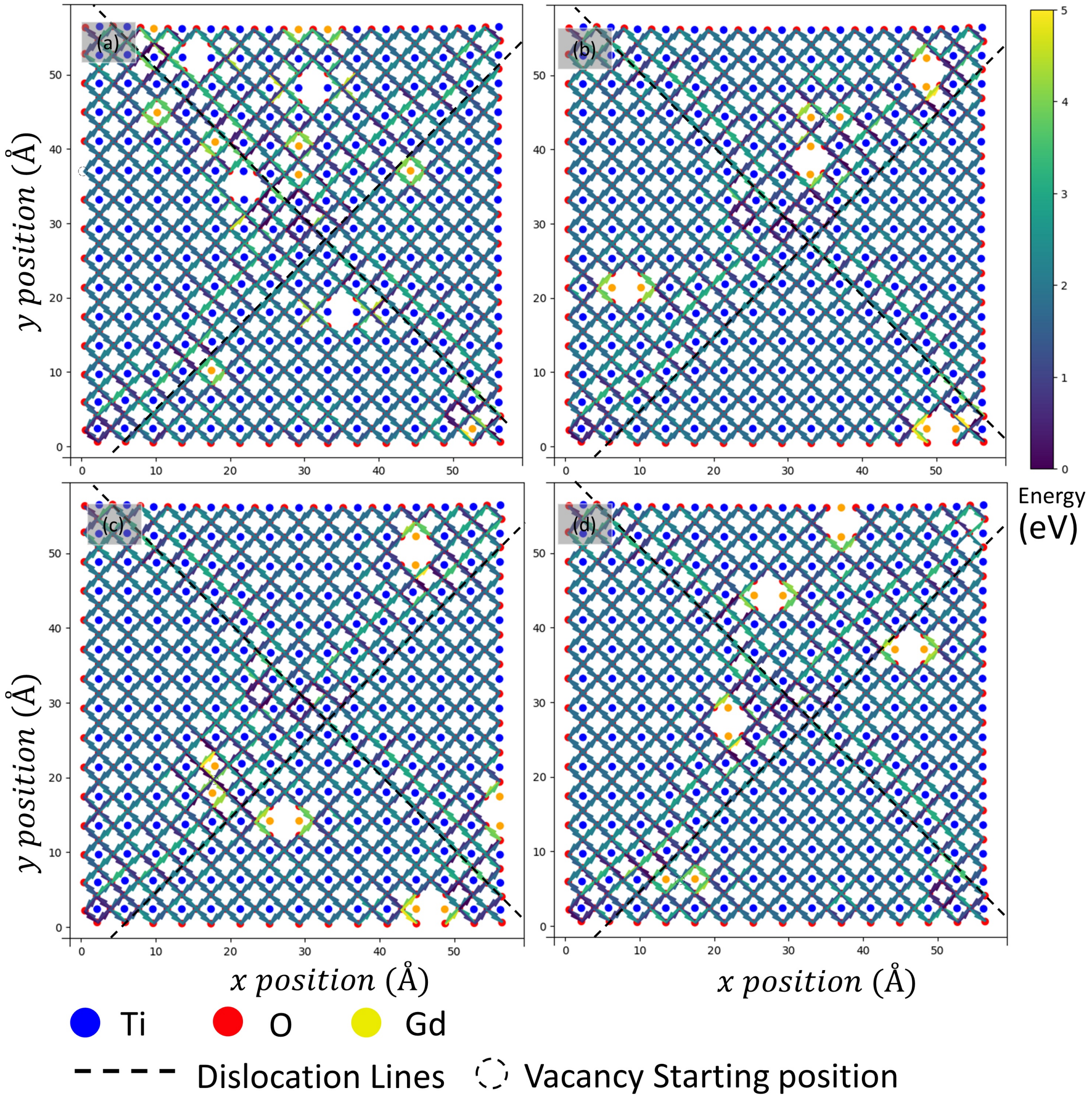

Figure 5 shows migration energy barriers at the TiO$_2$ termination layer of the TiO$_2$-NiO interface (**Figure 1b)**. In the coherent Stacking 3 shown in **Figure 1b**, the migration energy barriers remain consistent due to the uniform {Ni/O$_{STO}$} coordinating pair configuration, where the oxygen atoms from the TiO$_2$ align vertically with the cations from the NiO layer. For instance, in the interior of the stackings away from the misfit dislocations, the average migration energy barrier is around 1.84 eV. These pathways are represented by the transition {Ni/O$_{STO}$} → {Ni/O$_{STO}$}. This regular stacking explains the uniformity in the oxygen vacancy migration energy barriers within such coherent terraces. Since the TiO_2-NiO interface exhibits misfit dislocations in the $\langle 110 \rangle$ crystal direction (**Figure 1b**), the variation in barrier heights creates a distinct pattern along the $\langle 110 \rangle$ direction. This can be seen for vacancy migration in close proximity and parallel to the misfit dislocation lines, highlighted by the dashed lines, which exhibit slightly higher barrier energies as compared to vacancy migration within the coherent terraces. This can be attributed to the nearest neighbor environment along the misfit dislocation lines. More specifically, **Figure 1b** clearly highlights that along the misfit dislocation lines, the O_{STO} atoms belonging to the TiO_2 layer do not have a coordinating pair with any atomic species across the interface, yielding a $\{O_{STO}/[]\}$ nearest neighbor bonding, which explains the consistently higher energies for pathways parallel to the misfit dislocation lines. At the same time, the migration energy barriers for pathways away from the misfit dislocation lines are higher in magnitude as compared to the pathways towards the misfit dislocation lines, resulting in a repeating pattern for pathways orthogonal to the misfit dislocation lines. Thus, while migration of oxygen vacancies toward the misfit dislocations would be easier as shown by the transition from $\{O_{STO}/[]\} \rightarrow \{O_{STO}/[]\}$, they might get trapped in these regions due to the high thermal energy required to migrate away from the misfit dislocations. Similar oxygen vacancy segregation at structural defects has been observed in experimental studies[73]. It has been shown experimentally that oxygen vacancies in perovskite oxides tend to segregate towards the grain boundaries[73], with local strain and interfacial coordination environment playing a key role.

Figure 6. *Activation energy barriers for intra-layer oxygen vacancy defect migrations at the SrO-terminated layer of the SrO–NiO interface. In all the panels,* Gd^{3+} *dopants are isolated, with the total dopant and oxygen vacancy concentration consistent with previous configurations shown in* ***Figure 5***.

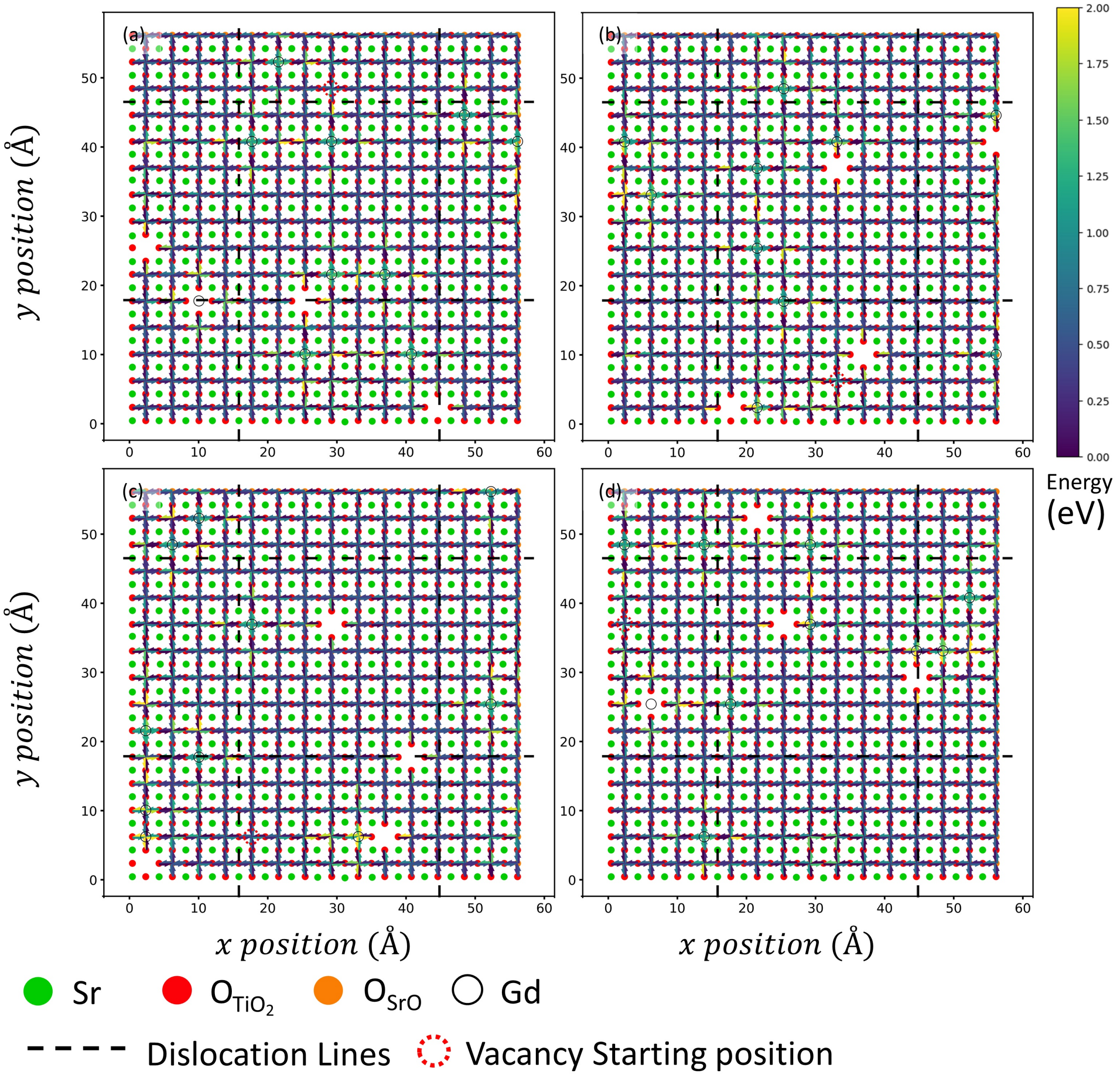

Figure 6 depicts the migration energy barriers at the SrO-terminated layer of the SrO-NiO interface (**Figure 1a)**. The migration barriers shown in **Figure 5** are for intra-layer migrations, meaning that the migration pathways shown are to and from the TiO_2 layer adjacent to the displayed SrO layer. As shown in **Figure 1a,** the SrO layer from SrO-NiO interface has two different stackings with different nearest neighbor coordination. The central stacking shown in **Figure 6** represents Stacking 2, and owing to the periodic boundary conditions, Stacking 1 is shown by the stackings to the right, left, top, and bottom of the central stacking. Closer inspection reveals that, similar to **Figure 5**, the migration energy barriers are distinct between the two stackings. Within a given stacking, the barriers are nearly identical, differing only marginally. However, barrier energies differ significantly among the two different stackings. This can again

be explained on the basis of the different nearest neighbor coordination. In Stacking 2, which is the central stacking in **Figure 6**, the oxygen atoms from the SrO layer have a nearest neighbor coordination given by $\{O_{STO}/O_{NiO}\}$, which means that the anions from both sides of the interface lie on top of each other in this particular stacking. On the other hand, for Stacking 1, the coordination is $\{O_{STO}/Ni\}$, implying that an anion from STO sits on top of the cation from the NiO interface. The electrostatic repulsion between the vertically aligned $\{O_{STO}/O_{NiO}\}$ anions at the interface in Stacking 2 weakens the overall oxygen binding environment. In Stacking 1, the electrostatically stable cation on an anion nearest neighbor coordination results in higher energy required for the transition of an oxygen ion from the TiO_2 layer to an oxygen vacancy in the SrO layer. This explains the lower migration energy barriers for oxygen vacancies moving out of the SrO layer in Stacking 2 as compared to those in Stacking 1. An exactly opposite picture is painted by the migrations toward the SrO layer from the TiO_2 layer. The migration energy barriers away or towards the misfit dislocation lines do not show any noticeable trends, as evident at the TiO_2-terminated layer of TiO_2-NiO interface (**Figure 5)**.

Figure 7. *Activation energy barriers for in-layer oxygen vacancy defect migrations at the NiO-terminated layer of the TiO_2–NiO interface. In all the panels, Gd^{3+} dopants are isolated, with the total dopant and oxygen vacancy concentration consistent with the previous configurations.*

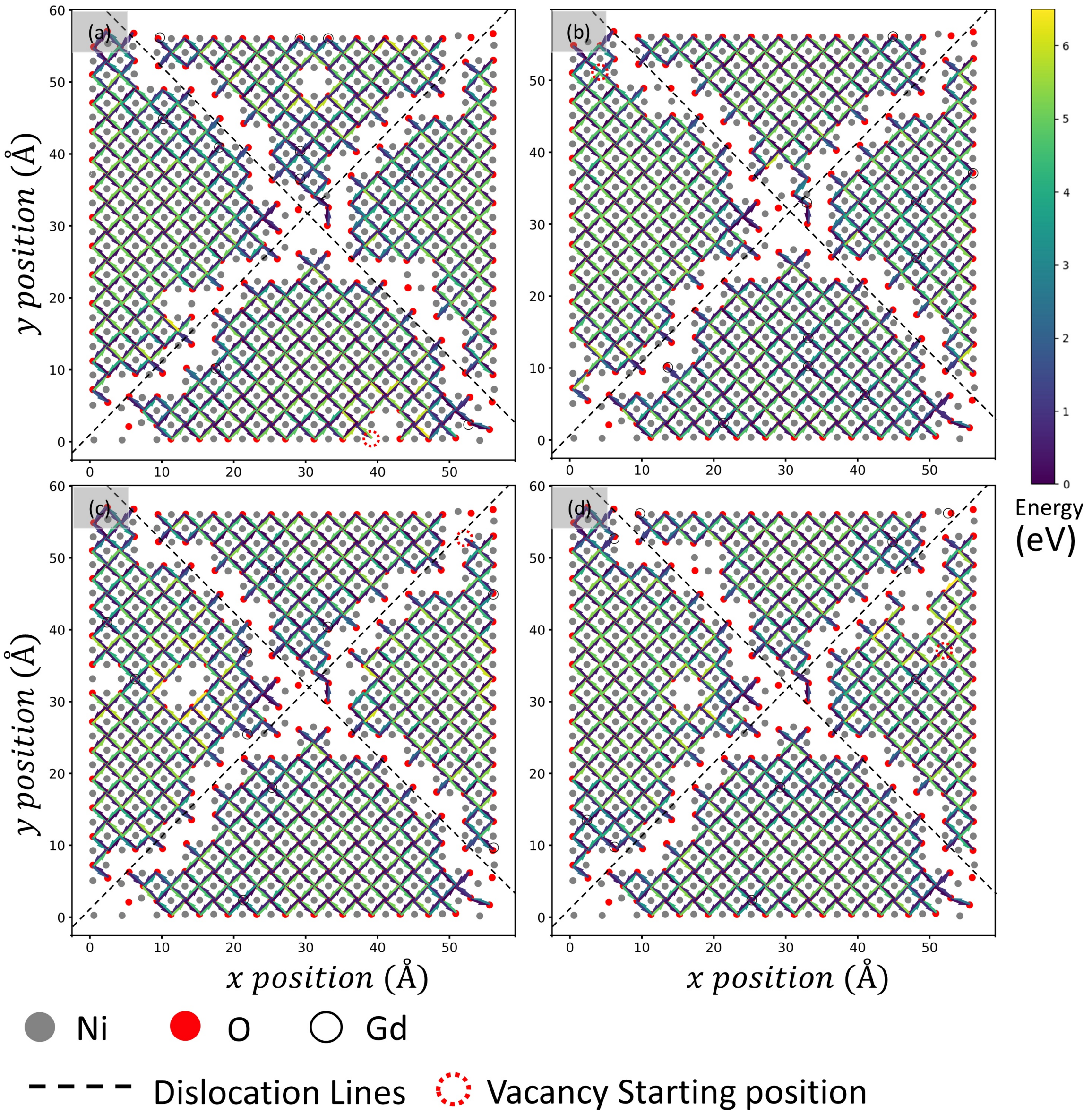

Figure 7 displays the migration energy barriers at the NiO-terminated layer of the TiO_2-NiO interface (**Figure 1b**). Since both in-layer and intra-layer migrations occur in the NiO layer (**Figure 4a)**, we focus on in-layer migrations at both TiO_2-NiO (**Figure 7**) and SrO-NiO (**Figure 9**) interfaces, with corresponding intra-layer migrations shown in **Figure 8** and **Figure 10. Figure 7** and **Figure 8** display the NiO layer from the same interface. For the coherent Stacking 3 in **Figure 7** and **Figure 8**, the nearest neighbor coordinating pairs for oxygen atoms in the NiO layer is given by $\{Ti/O_{NiO}\}$, and $[O_{NiO}]$. This creates an alternating atomic arrangement for the oxygen atoms in the NiO layer, where one column of oxygen atoms aligns vertically with Ti atoms across the interface, while the adjacent column is devoid of a coordinating pair across the interface. The

potential energy profile for the NiO interface from the TiO_2-NiO interface shown in **Supporting Information (SI) Figure 1a** clearly highlights this structural periodicity, with oxygen atoms showing alternating high and low potential energies between columns. This also explains the nature of the migration energy barriers in the coherent stackings for both the in-layer and intra-layer migrations. The transition from $\{Ti/O_{NiO}\} \rightarrow \{/[O_{NiO}]\}$ requires significantly less energy as compared to the reverse transition. In terms of the potential energy profile shown in **SI Figure 1a**, the isolated oxygen atoms have an inherently higher potential energy per atom as compared to the oxygen atoms having Ti atoms as the nearest coordinating atom, implying that a transition from $\{Ti/O_{NiO}\} \rightarrow [O_{NiO}]$ is much more favorable for an oxygen vacancy as compared to $[O_{NiO}] \rightarrow \{Ti/O_{NiO}\}$ (reverse jump), since the former would involve a net loss of energy for the oxygen atom undergoing the transition. This trend is much more evident in **Figure 7** as opposed to **Figure 8**, due to the zigzag atomic arrangement in the NiO layer along the *z*-axis near the TiO_2-NiO interface. This alternating elevation of oxygen atoms creates a grouping wherein those oxygen atoms located at lower *z*-coordinates become less accessible as nearest neighbor sites for vacancy hopping. This also explains why a lot of the intermittent oxygen atoms in **Figure 8** do not show any possible nearest neighbor migration pathways. Similar to **Figure 7**, though, the migration into the oxygen sites with no coordinating atoms is much easier as opposed to the migration into the oxygen sites with a nearest neighbor coordinating atom, which agrees well with experimental results[74].

As evident in **Figure 7**, despite having a similar nearest neighbor coordination environment throughout the interface, the migration barrier energies in the stackings adjacent to each other display a stark contrast. This contrast is depicted by the high density of migrations with lower activation energies in one group of stackings compared to the other, despite their identical nearest neighbor coordination environment. Even though strain fields at the interfacial level have not been quantified, the atomic rearrangements at misfit dislocations introduce strain in adjacent stackings. The stackings on the left and right, which, due to the periodic boundary conditions, constitute one single stacking, experience different local strain compared to those at the top and bottom, which form another periodic stacking. In this case, one stacking experiences tensile strain, lowering migration barrier energies, whereas the other experiences compressive strain, raising the activation energies. Strain has been shown to be fundamentally linked to oxygen vacancy formation energies and subsequently, oxygen vacancy diffusion throughout complex oxides[75].

Figure 8. *Activation energy barriers for intra-layer oxygen vacancy defect migrations at the NiO-terminated layer of the TiO_2–NiO interface. In all the panels, Gd^{3+} dopants are isolated, with the total dopant and oxygen vacancy concentration consistent with the previous configurations.*

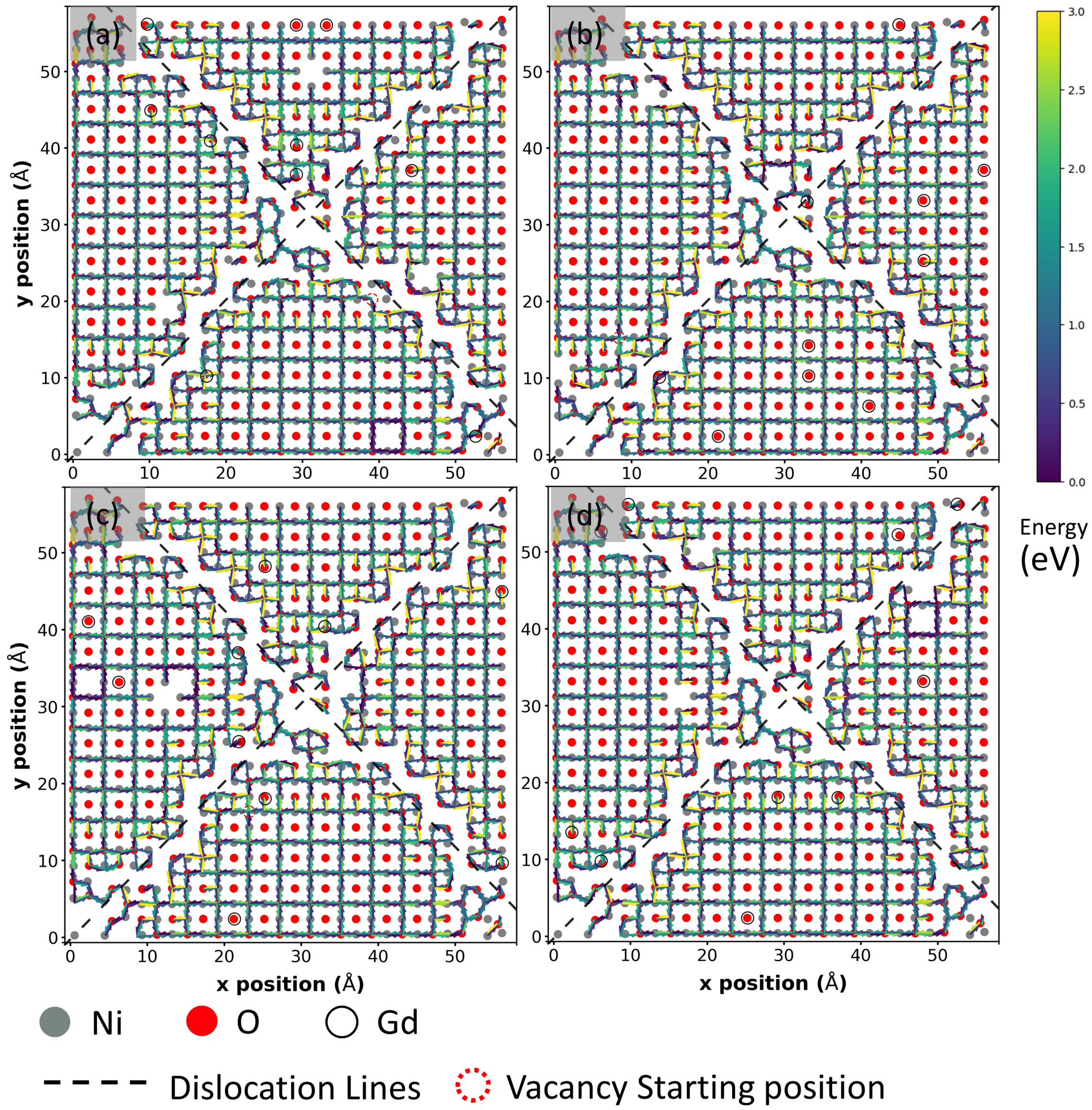

On the other hand, the activation energy barriers emerging at or near the misfit dislocation lines generate a discernible pattern. Again, at the TiO_2-NiO interface, the misfit dislocations running in the ⟨110⟩ crystal direction push the interface layer atoms away from them, leading to the formation of coherent patches in between and highly distorted misfit dislocation regions with additional local strain as compared to the coherent patches. This results in the formation of intermittent cavities along the misfit dislocations. Owing to the additional space available in these regions, the larger oxygen ions favor these regions and thus the activation energies for vacancy migration towards the misfit dislocation lines tend to be lower than those for vacancy migration away from the misfit dislocation lines, as shown in **Figure 8**. This makes the misfit dislocation lines act like thermodynamic sinks for oxygen vacancies, which could lead to vacancy aggregation. However, in the case of the in-layer vacancy migration depicted in **Figure 7,** the oxygen atoms having the nearest neighbor coordinating pair $\{/[O_{NiO}]\}$ within the coherent stackings are much more favorable as compared to vacancy migration towards the misfit dislocation lines, which is in contrast to the general trend. Prior studies have demonstrated a fundamental correlation between oxygen vacancy formation energy and oxygen vacancy migration barriers[76], though the exact relationship remains system-dependent. This can again be explained using the energy profile of the TiO_2-NiO (**SI Figure 1**) interface, as well as the oxygen vacancy formation energies along the misfit dislocation lines and in the coherent stackings. The potential energy per atom along the misfit dislocations is lower, whereas the oxygen vacancy formation energy is higher as compared to the values for the oxygen atoms in the $[O_{NiO}]$ position in the coherent stacking, thus explaining why the oxygen vacancies find the coherent stackings much more favorable as compared to the misfit dislocations.

Figure 9 and **Figure 10** show the migration energy barriers in the NiO layer from the SrO-NiO interface. In this interface, the misfit dislocations run in the $\langle 100 \rangle$ crystal direction. The coherent Stacking 1 and Stacking 2 again give rise to two distinct groups displaying unique migration energy barriers within each stacking. The nearest neighbor coordination pair for the oxygen atoms in Stacking 2 is given by $\{Sr/O_{NiO}\}$ and $\{O_{STO}/O_{NiO}\}$, whereas the same for oxygen atoms in Stacking 1 is given by $\{/[O_{NiO}]\}$. Similar to behavior observed in Stacking 3 in **Figure 7** and **Figure 8**, the alternate atomic arrangement of Sr- and O_{STO}-coordinated oxygen atoms in Stacking 2 results in a distinctive low-high value of activation energies, with the activation energies for vacancy migration towards the O_{STO}-coordinated oxygen sites being significantly lower as compared to the migrations towards the Sr-coordinated oxygen sites. This is also supported by the energy profile for the NiO layer at the SrO-NiO interface shown in **SI Figure 1c.** Stacking 1 contains only one type of nearest neighbor coordination pair, which results in almost uniform activation energies spread throughout the coherent stacking. On the other hand, there are no distinctive trends for migrations towards or away from the misfit dislocation lines.

Figure 9. *Activation energy barriers for in-layer oxygen vacancy defect migrations at the NiO-terminated layer of the SrO–NiO interface. In all the panels, Gd^{3+} dopants are isolated, with the total dopant and oxygen vacancy concentration consistent with the previous configurations.*

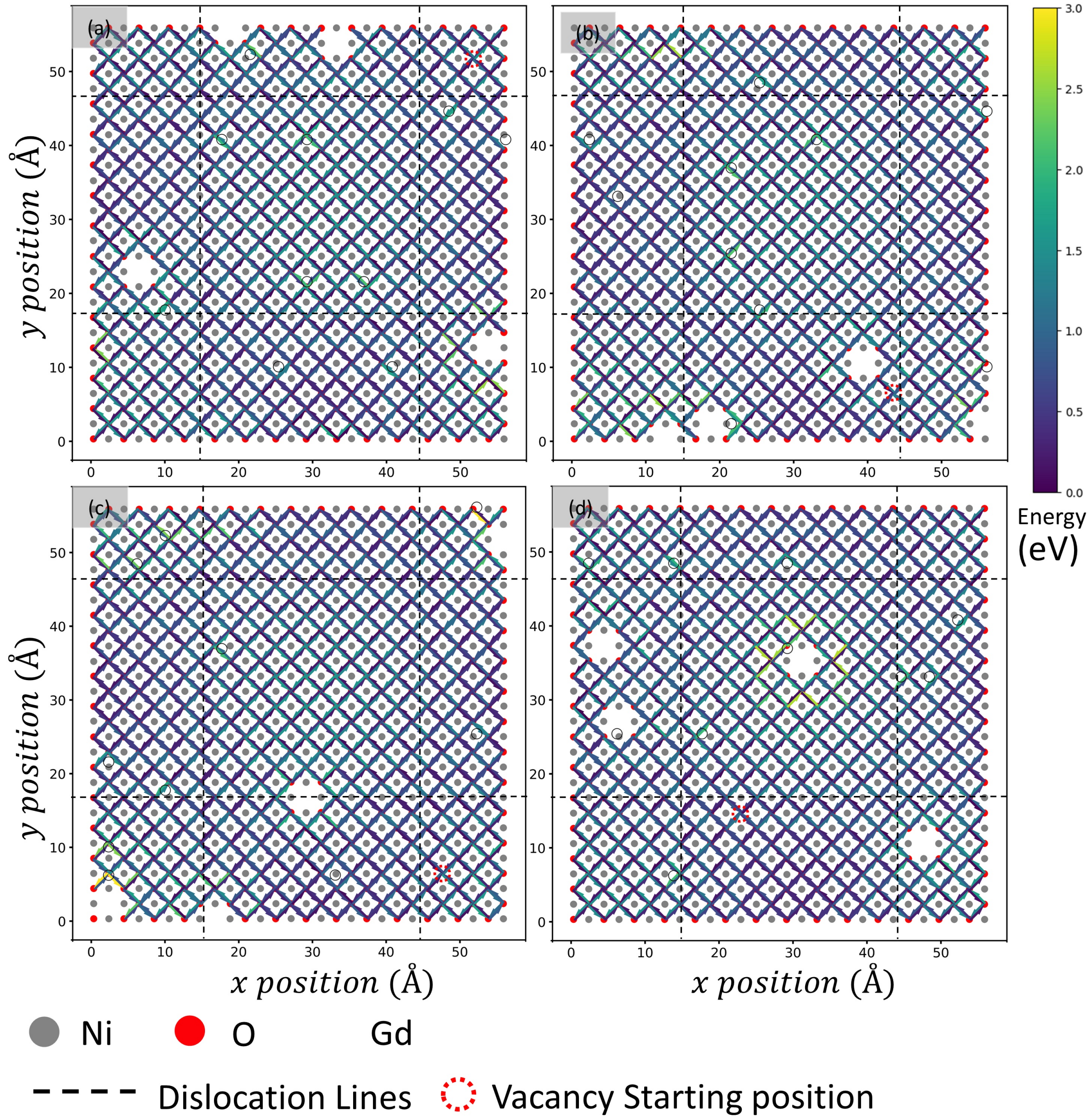

Figure 10. *Activation energy barriers for intra-layer oxygen vacancy defect migrations at the NiO-terminated layer of the SrO–NiO interface. In all the panels, Gd^{3+} dopants are isolated, with the total dopant and oxygen vacancy concentration consistent with the previous configurations.*

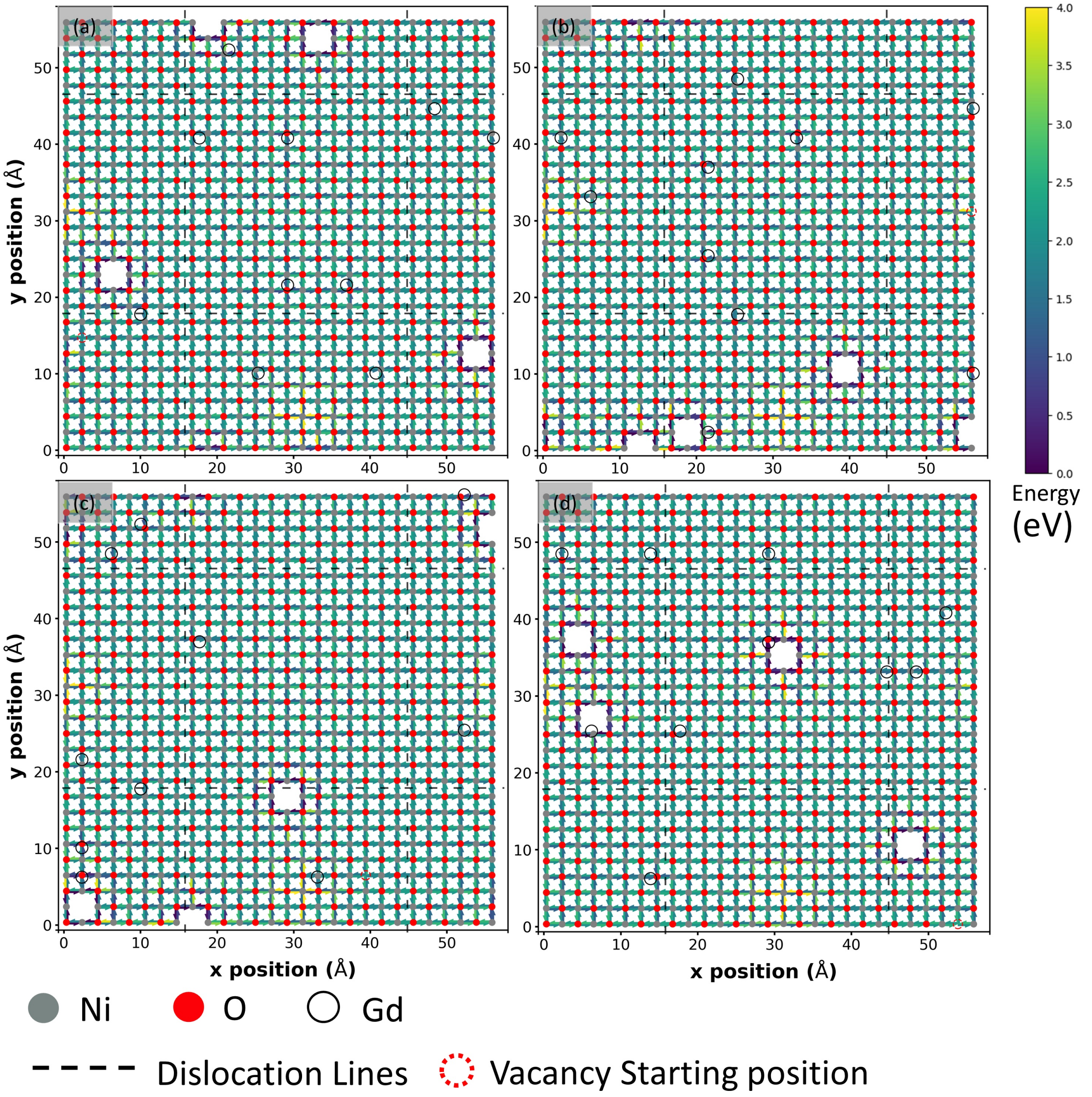

Figure 10 shows migration energy barriers consistent with the stacking patterns shown in **Figure 1a.** For pathways out of the interface layer, the activation energies in the coherent Stacking 1 are higher than the energies in the central coherent Stacking 2. A similar trend is noticed for the vacancy migration back into the interface layer, where Stacking 2 exhibits lower migration energy barriers as compared to the adjacent Stacking 1. Within Stacking 2, vacancy migration back into the interface layer exhibits a repeating high and low activation energy mirroring the NiO layer at the TiO_2-NiO interface. This can again be explained using the nearest neighbor environment across the interface for the oxygen atoms located in the coherent Stacking 2. The nearest neighbor

coordination pair for oxygen atoms in Stacking 2 is given by {Sr/O_{NiO}} and {O_{STO}/O_{NiO}}. This results in the formation of unstable pockets corresponding to the configuration {Sr/O_{NiO}}, which is surrounded by favorable zones, with lower activation energies corresponding to the configuration {O_{STO}/O_{NiO}}. **SI Figure 1c** corroborates this behavior, showing lower potential energy per atom at the {Sr/O_{NiO}} sites as compared to the {O_{STO}/O_{NiO}} sites, while Stacking 1 shows uniform potential energy per atom distribution. Together, these results indicate that Stacking 2 is conducive to intra-layer ionic transport as opposed to the coherent Stacking 1, which will have direct implications for ionic diffusion in the vicinity of misfit dislocations.

A common behavior uncovered across the various interfaces, as shown in **Figure 5-Figure 10**, is the impact of oxygen vacancies and dopants on the oxygen vacancy migration barriers. The migration energy barriers for the jumps towards the dopants are significantly lower than the hops away from the dopants, indicating that the oxygen vacancies will tend to get trapped around the dopants due to the high thermal energies required to escape such regions. The migration energy barriers around existing (stationary) oxygen vacancies depict a completely opposite picture. Owing to electrostatic interactions and vacancy-dopant association, oxygen vacancies have low activation energy barriers to hop towards the Gd^{3+} dopants in the coherent terrace but would require higher thermal energy to move out of the vacancy-dopant complex.

The density of atoms on both sides of the interface is different due to unequal expansion of the bulk material on either side of the interface. This affects the anion concentration at the interface region and also marginally influences the observed trends in oxygen vacancy migration energy barriers. Due to the preference of the oxygen vacancies that could potentially migrate towards the misfit dislocation lines and the corresponding lower oxygen vacancy formation energies in the vicinity of misfit dislocation, we expect a large fraction of the oxygen vacancies to segregate in this region or perhaps decorate the misfit dislocations. However, the higher values of migration energy barriers away from these regions will lower the probability of oxygen vacancies dynamically diffusing away from such regions. This could lead to contrasting results impacting ionic transport in the vicinity of misfit dislocations[55].

Figure 11. *Explicit plots of the migration barrier energies as a function of their distance from the nearest misfit dislocation lines for: (a) In-layer migrations at the* TiO_2*-terminated layer at the* TiO_2*-NiO interface, (b) Intra-layer migrations at the SrO-terminated layer at the SrO-NiO interface, (c) In-layer migrations at the NiO-terminated layer at the* TiO_2*-NiO interface, (d) Intra-*

layer migrations at the NiO-terminated layer at the TiO_2-NiO interface(e) In-layer migrations at the NiO-terminated layer at the SrO-NiO interface, and (f) Intra-layer migrations at the NiO-terminated layer at the SrO-NiO interface.

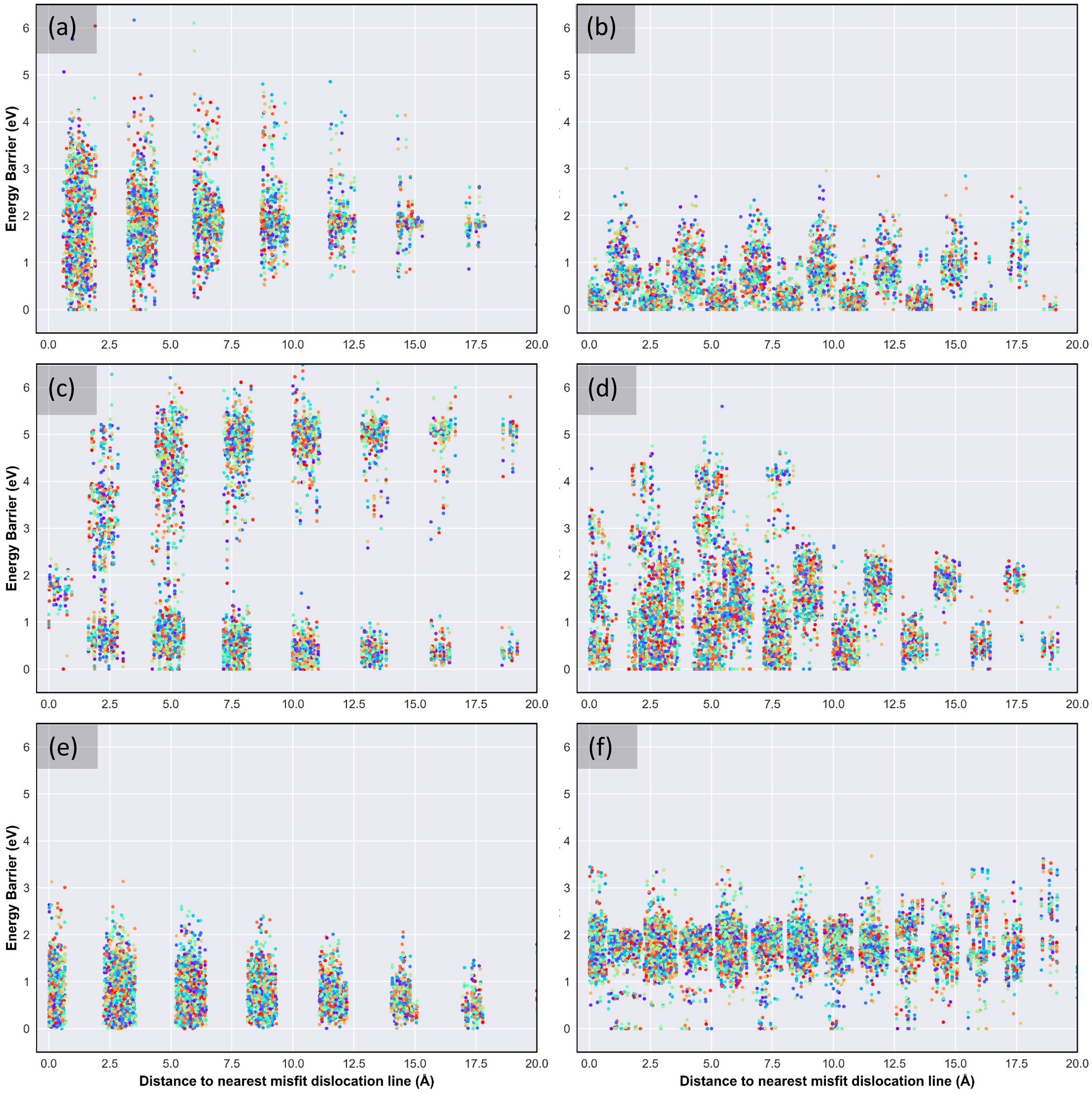

To further investigate the role of misfit dislocations in oxide ion migration and predict fundamental mechanisms, we examine the migration energy barriers across all interfaces as a function of their distance from the nearest dislocation line. The aggregated data for migration energy barriers from all four cases for the corresponding layers given in **Figure 5- Figure 10** is shown in **Figure 11**. The distance is calculated as the perpendicular distance between the transition line and the nearest misfit dislocation lines. Unlike the perovskite-perovskite heterostructures studied earlier[22], the perovskite-rocksalt heterostructure studied herein shows distinct interfacial dynamics. In the TiO_2 layer (**Figure 11a)**, migration energy barriers near misfit dislocation lines show a broad spread ranging from 0 eV to 4 eV that decreases with distance. The average migration energy barrier, 1.88 eV, is higher than the bulk values. However, this can be attributed to the absence of nearest neighbor coordinating pair across the interface for oxygen ions close to the misfit dislocations. Consequently, vacancy migration energy in such regions is found to be higher in magnitude as explained earlier, while the migration energy barriers away and towards the misfit dislocation lines alternate between high and low resulting in a large spread. Similar behavior is observed for **Figure 11b** and **Figure 11e**, wherein there is significant spread in the activation energies near misfit dislocations that decreases with distance. The average migration energy barrier in the SrO layer is 0.85eV, which is consistent with bulk values[77,78]. Similarly, for the NiO layer at the SrO-NiO interface, the average migration energy barrier is notably low (0.77 eV) despite the predicted higher energy barriers in NiO[79,80] due to the stronger ionic bonding in rocksalt oxides. This can be explained on the basis of the intrinsic strain[81] at the SrO-NiO interface, which leads to lower migration energy barriers. On the other hand, the in-layer and intra-layer migrations in the NiO layer at the NiO-TiO_2 interface exhibit dual band-like properties away from the misfit dislocations. This is due to the alternating low and high migration energy barriers within the coherent stackings. The average migration energy barriers for the in-layer and intra-layer jumps are 2.45 eV and 1.32 eV, respectively, which fall within the theoretical expectations. In general, trivalent dopants, interface layer chemistry, interface asymmetry, and availability of nearest neighbor hopping sites are some of the fundamental factors responsible for altering the migration energy barriers in the neighborhood of misfit dislocations.

This study tries to address knowledge gaps in the literature concerning ionic transport in mismatched oxide heterostructures and unravel the role of misfit dislocations. While misfit dislocations are ubiquitous in semi-coherent oxide heterostructures and are known to influence ionic transport, their influence on oxygen vacancy migration remains poorly understood. In literature, dislocations are often viewed as barriers or thermodynamic sinks, but their influence on ionic transport is not clear. Several experiments report that misfit dislocations can promote oxygen ion transport[9,10,82–86]. A few others report the exact opposite, indicating that dislocations hinder ionic diffusion[87–89]. A similar divide is noticed for computational studies[90]. This issue is compounded by the difficulty in visualizing oxygen vacancies experimentally[91,92]. On top of that, experimental work often focuses on perovskite-perovskite interfaces[93,94] neglecting the impact of dopant and vacancy clusters[23,95] on the activation energies.

This work predicts the accurate atomic-scale structure of misfit dislocations in STO/NiO and reports the broad distribution of oxygen vacancy migration energy barriers associated with different interface layer chemistries and nearest neighbor chemical environment. We show that misfit dislocation structure is contingent on the interface layer chemistry, which plays a vital role in modulating the oxygen vacancy migration in contrasting ways. That is, some interface layers facilitate oxide ion migration, while others impede vacancy motion, which will ultimately dictate ionic conductivity, highlighting the critical influence of local structural disorder. The results underpin the anomalous behavior of oxygen vacancy migration arising due to the presence of misfit dislocations in complex oxide heterostructures. How the interface layer chemistry and resulting misfit dislocation structure impacts ionic conductivity in a given oxide heterostructure could differ from another oxide heterostructure, which could be one of the fundamental factors accountable for reported conflicting results on ionic conductivity measurements. Fundamentally, most experiments do not report the precise termination layer chemistry or the prevailing misfit dislocation structure at oxide interfaces. Moreover, mixed terminations at oxide interfaces are likely to occur, which would further complicate the effects of termination layer chemistry. As a result, it is plausible that for a given thin film oxide electrolyte, different experiments are reporting ionic conductivities for different termination layer chemistries. For oxide heterostructures with mixed terminations, it is also probable that even in the same experiment, the conductivity values are representative of different interface layer chemistries and resulting misfit dislocation structures, which could potentially lead to discrepancies in reported values of ionic conductivities.

In our study, for example, the misfit dislocations at the TiO_2 termination layer of the STO/NiO heterostructure were found to hinder oxygen vacancy diffusion, as evidenced by the high migration barriers in regions away from the dislocation core. In contrast, the presence of SrO termination layers leads to markedly lower migration barrier energies, thereby promoting vacancy mobility. By identifying such local structural motifs and their corresponding effects on ion transport, our findings lay the theoretical foundation for selectively designing thin films that favor one interface over another to optimize ionic conductivity. This mechanistic understanding has been largely missing in the field[12,13] and this work helps bridging that gap.

These findings add further weight to the need to understand the intricate interplay between extended defects, dopants, and oxygen vacancies and how it governs the oxygen vacancy migration to enable the development of high-conductivity thin-film oxide electrolytes. However, it is critical to point out that oxygen vacancy migration energy barriers do not provide fundamental insights into diffusion kinetics, but they offer a starting point to study diffusion kinetics. In the near future, we plan to feed these computed nearest neighbor activation energies into the kinetic lattice Monte Carlo (KLMC) model[22,96], developed by the co-authors, to study oxygen vacancy diffusion at oxide heterointerfaces as a function of interface layer chemistry, temperature, and dopant fraction, which will facilitate the determination of ionic conductivity. Although simulations herein are conducted at 0 K, the temperature dependence of the oxygen vacancy diffusion will be studied using the KLMC model, wherein the Arrhenius equation governs the probabilities associated with vacancy diffusion. KLMC models have the predictive power to facilitate material design, and thus, high-throughput data from this work will serve as groundwork for future design of next-generation thin film oxide electrolytes. In our previous work, we employed a similar strategy to study and design bulk oxide electrolyte materials as well as compare their performance with experimental observations[96]. In addition, such high-throughput data can also be utilized to study the mean first passage time for an oxygen vacancy to travel between two distinct points in the heterostructure[97].

4. Conclusions

This work addresses critical knowledge gaps in the literature related to the lack of understanding of ionic transport across oxide heterointerfaces, particularly those containing misfit dislocations. Using a high-throughput NEB-based framework, we have shown how oxygen vacancy migration barriers are modulated by local coordination environment and interfacial chemistry in lattice-mismatched perovskite-rocksalt heterostructures. Basic outcomes in this work reveal that misfit dislocations are not passive sinks, but chemically complex and structurally distinct regions that alter oxygen vacancy migration, and as a result, are likely to impact ionic diffusion. We demonstrated the tendency of misfit dislocations to exhibit directionally dependent migration behavior; however, even such behavior is heavily dependent on the interface chemistry and nearest neighbor chemical environment. Thus, these insights not only assist in identifying the basic reasons for conflicting reports in literature but also highlight the need to account for extended defect structures, dopant interactions, and layer-specific chemistry in future models of ionic transport. By capturing these effects, this study lays the groundwork for facilitating the design of high-performance SOFCs, where control over defect-driven transport is key to functionality and efficiency.

Conflicts of interest: There are no conflicts to declare.

Author contributions: A. M. developed the high-throughput nudged elastic band framework and performed all atomistic simulations under the supervision of P. P. D., who conceptualized the study. W. E. provided input in the development of high-throughput framework. A. M. wrote the initial draft of the manuscript. All authors discussed and provided input on writing the final version of the manuscript.

Supporting Information: Figures for high-throughput NEB algorithm and potential energy profile analysis for interface layers in STO/NiO heretostructure.

Acknowledgements

This work is supported by the National Science Foundation (NSF) CAREER Award grant number DMR-2042311 in the Division of Materials Research. The authors acknowledge Research Computing at the Rochester Institute of Technology for providing computational resources and support that have contributed to the research results reported in this publication. This work used Expanse Cluster at San Diego Supercomputer Center through allocation PHY180045 from the Advanced Cyberinfrastructure Coordination Ecosystem: Services & Support (ACCESS) program, which is supported by NSF grants 2138259, 2138286, 2138307, 2137603, and 2138296.

References

[1] Q. Wang, H. Fan, Y. Xiao, and Y. Zhang, “Applications and recent advances of rare earth in solid oxide fuel cells,” J. Rare Earths **40**, 1668–1681 (2022).

[2] P. Boldrin, and N.P. Brandon, “Progress and outlook for solid oxide fuel cells for transportation applications,” Nat. Catal. **2**(7), 571–577 (2019).

[3] C.-H. Ma, J. Jiang, P.-W. Shao, Q.-X. Peng, C.-W. Huang, P.-C. Wu, J.-T. Lee, Y.-H. Lai, D.-P. Tsai, J.-M. Wu, S.-C. Lo, W.-W. Wu, Y.-C. Zhou, P.-W. Chiu, and Y.-H. Chu, “Transparent Antiradiative Ferroelectric Heterostructure Based on Flexible Oxide Heteroepitaxy,” ACS Appl. Mater. Interfaces **10**(36), 30574–30580 (2018).

[4] Z. Ren, Y. Guo, C.-H. Liu, and P.-X. Gao, “Hierarchically nanostructured materials for sustainable environmental applications,” Front. Chem. **1**, (2013).

[5] Y. Li, W. Wang, D. Zhang, M. Baskin, A. Chen, S. Kvatinsky, E. Yalon, and L. Kornblum, “Scalable $\rm Al_2O_3-TiO_2$ Conductive Oxide Interfaces as Defect Reservoirs for Resistive Switching Devices,” Adv. Electron. Mater. **9**(2), (2023).

[6] E. Assmann, P. Blaha, R. Laskowski, K. Held, S. Okamoto, and G. Sangiovanni, “Oxide Heterostructures for Efficient Solar Cells,” Phys. Rev. Lett. **110**(7), (2013).

[7] P. Zubko, S. Gariglio, M. Gabay, P. Ghosez, and J.-M. Triscone, “Interface Physics in Complex Oxide Heterostructures,” Annu. Rev. Condens. Matter Phys. **2**(1), 141–165 (2011).

[8] Y. Dong, M. Yousaf, M.A.K.Y. Shah, M. Akbar, Y. Lu, L. Zhang, Q.A. Sial, P. Cao, and C. Deng, “Developing CeO2-CoAl2O4 Semiconductor Ionic Based Heterostructure Composite Electrolyte for Low-Temperature Solid Oxide Fuel Cells (SOFCs),” Crystals **13**(6), 975 (2023).

[9] E. Fabbri, D. Pergolesi, and E. Traversa, “Ionic conductivity in oxide heterostructures: the role of interfaces,” Sci. Technol. Adv. Mater. **11**(5), 054503 (2010).

[10] J. Garcia-Barriocanal, A. Rivera-Calzada, M. Varela, Z. Sefrioui, E. Iborra, C. Leon, S.J. Pennycook, and J. Santamaria, “Colossal Ionic Conductivity at Interfaces of Epitaxial ZrO2:Y2O3/SrTiO3 Heterostructures,” Science **321**(5889), 676–680 (2008).

[11] P. Wang, W. Yi, J. Chen, S. Ito, C. Cui, and T. Sekiguchi, “Oxygen vacancy migration along dislocations in SrTiO3 studied by cathodoluminescence,” J. Phys. Appl. Phys. **52**(47), 475103 (2019).

[12] V. Metlenko, A.H.H. Ramadan, F. Gunkel, H. Du, H. Schraknepper, S. Hoffmann-Eifert, R. Dittmann, R. Waser, and R.A.D. Souza, “Do dislocations act as atomic autobahns for oxygen in the perovskite oxide SrTiO3?,” Nanoscale **6**(21), 12864–12876 (2014).

[13] L. Sun, D. Marrocchelli, and B. Yildiz, “Edge dislocation slows down oxide ion diffusion in doped CeO2 by segregation of charged defects,” Nat. Commun. **6**(1), 6294 (2015).

[14] K.P. Koirala, M.D. Hossain, L. Wang, Z. Zhuo, W. Yang, M.E. Bowden, S.R. Spurgeon, C. Wang, P.V. Sushko, and Y. Du, “Layer Resolved Cr Oxidation State Modulation in Epitaxial SrFe0.67Cr0.33O3−δ Thin Films,” Nano Lett. **24**(45), 14244–14251 (2024).

[15] H. He, Z. Yang, Y. Xu, A.T. Smith, G. Yang, and L. Sun, “Perovskite oxides as transparent semiconductors: a review,” Nano Converg. **7**(1), 32 (2020).

[16] Y. Liu, H. Huang, L. Xue, J. Sun, X. Wang, P. Xiong, and J. Zhu, “Recent advances in the heteroatom doping of perovskite oxides for efficient electrocatalytic reactions,” Nanoscale **13**(47), 19840–19856 (2021).

[17] A. Chroneos, I.L. Goulatis, A. Solovjov, and R.V. Vovk, “The Evolution of Solid Oxide Fuel Cell Materials,” Appl. Sci. **14**(1), 69 (2024).

[18] W. Luo, W. Duan, S.G. Louie, and M.L. Cohen, “Structural and electronic properties of n -doped and p -doped Sr Ti O 3,” Phys. Rev. B **70**(21), 214109 (2004).
[19] Y. Duan, “Electronic structural, optical and phonon lattice dynamical properties of pure- and La-doped SrTiO 3 : An ab initio thermodynamics study,” J. Solid State Chem., (2017).
[20] D. Neagu, and J.T.S. Irvine, “Enhancing Electronic Conductivity in Strontium Titanates through Correlated A and B-Site Doping,” Chem. Mater. **23**(6), 1607–1617 (2011).
[21] H.-I. Yoon, D.-K. Lee, H.B. Bae, G.-Y. Jo, H.-S. Chung, J.-G. Kim, S.-J.L. Kang, and S.-Y. Chung, “Probing dopant segregation in distinct cation sites at perovskite oxide polycrystal interfaces,” Nat. Commun. **8**(1), 1417 (2017).
[22] W. Ebmeyer, and P.P. Dholabhai, “High-throughput prediction of oxygen vacancy defect migration near misfit dislocations in SrTiO3/BaZrO3 heterostructures,” Mater. Adv. **5**(1), 315–328 (2024).
[23] T.T. Mayeshiba, and D.D. Morgan, “Factors controlling oxygen migration barriers in perovskites,” Solid State Ion. **296**, 71–77 (2016).
[24] M. Cherry, M.S. Islam, and C.R.A. Catlow, “Oxygen Ion Migration in Perovskite-Type Oxides,” J. Solid State Chem. **118**(1), 125–132 (1995).
[25] E. Gilardi, E. Fabbri, L. Bi, J.L.M. Rupp, T. Lippert, D. Pergolesi, and E. Traversa, “Effect of Dopant–Host Ionic Radii Mismatch on Acceptor-Doped Barium Zirconate Microstructure and Proton Conductivity,” J. Phys. Chem. C **121**(18), 9739–9747 (2017).
[26] C. Ohly, S. Hoffmann-Eifert, K. Szot, and R. Waser, “Electrical conductivity and segregation effects of doped SrTiO3 thin films,” J. Eur. Ceram. Soc. **21**(10), 1673–1676 (2001).
[27] S. Zhao, L. Gao, C. Lan, S.S. Pandey, S. Hayase, and T. Ma, “Oxygen vacancy formation and migration in double perovskite Sr2CrMoO6: a first-principles study,” RSC Adv. **6**(49), 43034–43040 (2016).
[28] J.M. Azpiroz, E. Mosconi, J. Bisquert, and F.D. Angelis, “Defect migration in methylammonium lead iodide and its role in perovskite solar cell operation,” Energy Environ. Sci. **8**(7), 2118–2127 (2015).
[29] M. Nolan, J.E. Fearon, and G.W. Watson, “Oxygen vacancy formation and migration in ceria,” Solid State Ion. **177**(35), 3069–3074 (2006).
[30] A. Kyrtsos, M. Matsubara, and E. Bellotti, “Migration mechanisms and diffusion barriers of vacancies in Ga 2 O 3,” Phys. Rev. B **95**(24), 245202 (2017).
[31] T. Norby, “Solid-state protonic conductors: principles, properties, progress and prospects,” Solid State Ion. **125**(1), 1–11 (1999).
[32] C. Noguera, *Physics and Chemistry at Oxide Surfaces* (Cambridge University Press, Cambridge, 1996).
[33] J.A. Kilner, and M. Burriel, “Materials for Intermediate-Temperature Solid-Oxide Fuel Cells,” Annu. Rev. Mater. Res. **44**(Volume 44, 2014), 365–393 (2014).
[34] B. Henderson, *Defects in the Alkaline Earth Oxides : With Applications to Radiation Damage and Catalysis* (London : Taylor & Francis ; New York : Halsted Press Division, J. Wiley, 1977).
[35] S. Plimpton, “Fast Parallel Algorithms for Short-Range Molecular Dynamics,” J. Comput. Phys. **117**(1), 1–19 (1995).
[36] R.A. Buckingham, and J.E. Lennard-Jones, “The classical equation of state of gaseous helium, neon and argon,” Proc. R. Soc. Lond. Ser. Math. Phys. Sci. **168**(933), 264–283 (1997).
[37] P.P. Ewald, “Die Berechnung optischer und elektrostatischer Gitterpotentiale,” Ann. Phys. **369**(3), 253–287 (1921).

[38] M. Deserno, and C. Holm, "How to mesh up Ewald sums. I. A theoretical and numerical comparison of various particle mesh routines," J. Chem. Phys. **109**(18), 7678–7693 (1998).
[39] G. Busker, A. Chroneos, R.W. Grimes, and I.-W. Chen, "Solution Mechanisms for Dopant Oxides in Yttria," J. Am. Ceram. Soc. **82**(6), 1553–1559 (1999).
[40] M.O. Zacate, L. Minervini, D.J. Bradfield, R.W. Grimes, and K.E. Sickafus, "Defect cluster formation in M2O3-doped cubic ZrO2," Solid State Ion. **128**(1), 243–254 (2000).
[41] L. Minervini, R.W. Grimes, J.A. Kilner, and K.E. Sickafus, "Oxygen migration in La2NiO4 + δ," J. Mater. Chem. **10**(10), 2349–2354 (2000).
[42] R.W. Grimes, D.J. Binks, and A.B. Lidiard, "The extent of zinc oxide solution in zinc chromate spinel," Philos. Mag. A **72**(3), 651–668 (1995).
[43]"Influence of Chemistry and Misfit Dislocation Structure on Dopant Segregation at Complex Oxide Heterointerfaces - Dholabhai - 2019 - Advanced Theory and Simulations - Wiley Online Library," (n.d.).
[44] P.P. Dholabhai, G. Pilania, J.A. Aguiar, A. Misra, and B.P. Uberuaga, "Termination chemistry-driven dislocation structure at SrTiO3/MgO heterointerfaces," Nat. Commun. **5**(1), 5043 (2014).
[45] P.P. Dholabhai, E. Martínez, N.T. Brown, and B.P. Uberuaga, "On the mobility of carriers at semi-coherent oxide heterointerfaces," Phys. Chem. Chem. Phys. PCCP **19**(34), 23122–23130 (2017).
[46] P.P. Dholabhai, J.A. Aguiar, A. Misra, and B.P. Uberuaga, "Defect interactions with stepped $CeO_2/SrTiO_3$ interfaces: implications for radiation damage evolution and fast ion conduction," J. Chem. Phys. **140**(19), 194701 (2014).
[47] P.P. Dholabhai, and B.P. Uberuaga, "Beyond Coherent Oxide Heterostructures: Atomic-Scale Structure of Misfit Dislocations," Adv. Theory Simul. **2**(9), 1900078 (2019).
[48] G. Pilania, P.P. Dholabhai, and B.P. Uberuaga, "Role of Symmetry, Geometry, and Termination Chemistry on Misfit Dislocation Patterns at Semicoherent Heterointerfaces," Matter **2**(5), 1324–1337 (2020).
[49] H. Zhao, F. Gao, X. Li, C. Zhang, and Y. Zhao, "Electrical properties of yttrium doped strontium titanate with A-site deficiency as potential anode materials for solid oxide fuel cells," Solid State Ion. **180**(2), 193–197 (2009).
[50] X. Ma, Y. Dai, M. Li, and B. Huang, "Oxygen vacancies at the Au/SrTiO3(001) interface: stabilities, electronic properties and effect on photocatalysis," Phys. Chem. Chem. Phys. **19**(1), 774–781 (2016).
[51] N.A. Richter, S. Sicolo, S.V. Levchenko, J. Sauer, and M. Scheffler, "Concentration of Vacancies at Metal-Oxide Surfaces: Case Study of MgO(100)," Phys. Rev. Lett. **111**(4), 045502 (2013).
[52] P.P. Dholabhai, "Oxygen Vacancy Formation and Interface Charge Transfer at Misfit Dislocations in Gd-Doped CeO2/MgO Heterostructures," J. Phys. Chem. C **126**(28), 11735–11750 (2022).
[53] P.P. Dholabhai, "Atomic-scale structure of misfit dislocations in CeO2/MgO heterostructures and thermodynamic stability of dopant–defect complexes at the heterointerface," Phys. Chem. Chem. Phys. **21**(37), 20878–20891 (2019).
[54] C. Marzano, and P.P. Dholabhai, "High-Throughput Prediction of Thermodynamic Stabilities of Dopant-Defect Clusters at Misfit Dislocations in Perovskite Oxide Heterostructures," J. Phys. Chem. C **127**(32), 15988–15999 (2023).

[55] W. Ebmeyer, P. Hatton, B. P. Uberuaga, and P. P. Dholabhai, “Influence of misfit dislocations on ionic conductivity at oxide interfaces,” J. Mater. Chem. A **12**(32), 21252–21267 (2024).

[56] Md.M. Hasan, P.P. Dholabhai, R.H.R. Castro, and B.P. Uberuaga, “Stabilization of MgAl2O4 spinel surfaces via doping,” Surf. Sci. **649**, 138–145 (2016).

[57] J.A. Aguiar, P.P. Dholabhai, Z. Bi, Q. Jia, E.G. Fu, Y.Q. Wang, T. Aoki, J. Zhu, A. Misra, and Blas.P. Uberuaga, “Linking Interfacial Step Structure and Chemistry with Locally Enhanced Radiation-Induced Amorphization at Oxide Heterointerfaces,” Adv. Mater. Interfaces **1**(4), 1300142 (2014).

[58] P.P. Dholabhai, J.A. Aguiar, L. Wu, T.G. Holesinger, T. Aoki, R.H.R. Castro, and B.P. Uberuaga, “Structure and segregation of dopant–defect complexes at grain boundaries in nanocrystalline doped ceria,” Phys. Chem. Chem. Phys. **17**(23), 15375–15385 (2015).

[59] R. Perriot, P.P. Dholabhai, and B.P. Uberuaga, “Disorder-induced transition from grain boundary to bulk dominated ionic diffusion in pyrochlores,” Nanoscale **9**(20), 6826–6836 (2017).

[60] M.M. Hasan, P.P. Dholabhai, S. Dey, B.P. Uberuaga, and R.H.R. Castro, “Reduced grain boundary energies in rare-earth doped MgAl2O4 spinel and consequent grain growth inhibition,” J. Eur. Ceram. Soc. **37**(13), 4043–4050 (2017).

[61] H. J?nsson, G. Mills, and K.W. Jacobsen, “Nudged elastic band method for finding minimum energy paths of transitions,” in *Class. Quantum Dyn. Condens. Phase Simul.*, (WORLD SCIENTIFIC, 1998), pp. 385–404.

[62] G. Mills, H. Jónsson, and G.K. Schenter, “Reversible work transition state theory: application to dissociative adsorption of hydrogen,” Surf. Sci. **324**(2), 305–337 (1995).

[63] G. Henkelman, and H. Jónsson, “Improved tangent estimate in the nudged elastic band method for finding minimum energy paths and saddle points,” J. Chem. Phys. **113**(22), 9978–9985 (2000).

[64] R. Takahashi, Y. Matsumoto, T. Ohsawa, M. Lippmaa, M. Kawasaki, and H. Koinuma, “Growth dynamics of the epitaxial SrO film on SrTiO3(0 0 1),” J. Cryst. Growth **234**(2), 505–508 (2002).

[65] Y. Zhu, C. Song, A.M. Minor, and H. Wang, “Cs-corrected scanning transmission electron microscopy investigation of dislocation core configurations at a SrTiO(3)/MgO heterogeneous interface,” Microsc. Microanal. Off. J. Microsc. Soc. Am. Microbeam Anal. Soc. Microsc. Soc. Can. **19**(3), 706–715 (2013).

[66] J.A. Aguiar, M. Zhuo, Z. Bi, E. Fu, Y. Wang, P.P. Dholabhai, A. Misra, Q. Jia, and B.P. Uberuaga, “Orientation-specific amorphization and intercalated recrystallization at ion-irradiated SrTiO3/MgO interfaces,” J. Mater. Res. **29**(16), 1699–1710 (2014).

[67] Y. Zhu, and M. Li, “Bipolar Resistive Switching Characteristic of Epitaxial NiO Thin Film on Nb-Doped SrTiO3 Substrate,” Adv. Condens. Matter Phys. **2012**(1), 364376 (2012).

[68] J.J. Brown, Z. Ke, W. Geng, and A.J. Page, “Oxygen Vacancy Defect Migration in Titanate Perovskite Surfaces: Effect of the A-Site Cations,” J. Phys. Chem. C **122**(26), 14590–14597 (2018).

[69] L. Zhang, B. Liu, H. Zhuang, P.R.C. Kent, V.R. Cooper, P. Ganesh, and H. Xu, “Oxygen vacancy diffusion in bulk SrTiO3 from density functional theory calculations,” Comput. Mater. Sci. **118**, 309–315 (2016).

[70] M. Schie, A. Marchewka, T. Müller, R.A. De Souza, and R. Waser, “Molecular dynamics simulations of oxygen vacancy diffusion in SrTiO3,” J. Phys. Condens. Matter **24**(48), 485002 (2012).

[71] J. Claus, M. Leonhardt, and J. Maier, "Tracer diffusion and chemical diffusion of oxygen in acceptor doped SrTiO3," J. Phys. Chem. Solids **61**(8), 1199–1207 (2000).
[72] B.P. Uberuaga, and L.J. Vernon, "Interstitial and vacancy mediated transport mechanisms in perovskites: A comparison of chemistry and potentials," Solid State Ion. **253**, 18–26 (2013).
[73] R.F. Klie, and N.D. Browning, "Atomic Scale Characterization of Oxygen Vacancy Segregation at SrTiO3 Grain Boundaries," MRS Online Proc. Libr. **654**(1), 171 (2000).
[74] V. Metlenko, A.H.H. Ramadan, F. Gunkel, H. Du, H. Schraknepper, S. Hoffmann-Eifert, R. Dittmann, R. Waser, and R.A. De Souza, "Do dislocations act as atomic autobahns for oxygen in the perovskite oxide $SrTiO_3$?," Nanoscale **6**(21), 12864–12876 (2014).
[75] T. Mayeshiba, and D. Morgan, "Strain effects on oxygen vacancy formation energy in perovskites," Solid State Ion. **311**, 105–117 (2017).
[76] S.-L. Shang, B.-C. Zhou, W.Y. Wang, A.J. Ross, X.L. Liu, Y.-J. Hu, H.-Z. Fang, Y. Wang, and Z.-K. Liu, "A comprehensive first-principles study of pure elements: Vacancy formation and migration energies and self-diffusion coefficients," Acta Mater. **109**, 128–141 (2016).
[77] A. Kushima, and B. Yildiz, "Role of lattice strain and defect chemistry on the oxygen vacancy migration at the (8.3%Y2O3-ZRO2)/SrTiO3 hetero-interface: A first principles study," MIT Web Domain, (2009).
[78] W. Sitaputra, N. Sivadas, M. Skowronski, D. Xiao, and R.M. Feenstra, "Oxygen vacancies on SrO-terminated $\mathrm{SrTi}{\mathrm{O}}_{3}(001)$ surfaces studied by scanning tunneling spectroscopy," Phys. Rev. B **91**(20), 205408 (2015).
[79] J.B. Wagner, "Electrical Conductivity, Diffusion, and Minority Defects in some Transition-Metal Oxides," in *Defects Transp. Oxides*, edited by M.S. Seltzer and R.I. Jaffee, (Springer US, Boston, MA, 1974), pp. 283–301.
[80] J. Yu, K.M. Rosso, and S.M. Bruemmer, "Charge and Ion Transport in NiO and Aspects of Ni Oxidation from First Principles," J. Phys. Chem. C **116**(2), 1948–1954 (2012).
[81] L. Iglesias, A. Gómez, M. Gich, and F. Rivadulla, "Tuning Oxygen Vacancy Diffusion through Strain in SrTiO3 Thin Films," ACS Appl. Mater. Interfaces **10**(41), 35367–35373 (2018).
[82] A. Peters, C. Korte, D. Hesse, N. Zakharov, and J. Janek, "Ionic conductivity and activation energy for oxygen ion transport in superlattices — The multilayer system CSZ (ZrO2 + CaO) / Al2O3," Solid State Ion. **178**(1), 67–76 (2007).
[83] M. Sillassen, P. Eklund, N. Pryds, E. Johnson, U. Helmersson, and J. Bøttiger, "Low-Temperature Superionic Conductivity in Strained Yttria-Stabilized Zirconia," Adv. Funct. Mater. **20**(13), 2071–2076 (2010).
[84] S.M. Yang, S. Lee, J. Jian, W. Zhang, P. Lu, Q. Jia, H. Wang, T. Won Noh, S.V. Kalinin, and J.L. MacManus-Driscoll, "Strongly enhanced oxygen ion transport through samarium-doped CeO2 nanopillars in nanocomposite films," Nat. Commun. **6**(1), 8588 (2015).
[85] Y. Saito, J. Cheng, K. Crabb, H. Huang, R. Pornprasertsuk, P.C. Su, and F. Prinz, "Ion Conductivity Enhancement Effect by Introduction of Dislocations in Yttria-Stabilized Zirconia," ECS Trans. **11**(33), 3–8 (2008).
[86] S. Lee, W. Zhang, F. Khatkhatay, H. Wang, Q. Jia, and J.L. MacManus-Driscoll, "Ionic Conductivity Increased by Two Orders of Magnitude in Micrometer-Thick Vertical Yttria-Stabilized ZrO 2 Nanocomposite Films," Nano Lett. **15**(11), (2015).
[87] X. Guo, "Comment on 'Colossal Ionic Conductivity at Interfaces of Epitaxial ZrO2:Y2O3/SrTiO3 Heterostructures,'" Science **324**(5926), 465–465 (2009).

[88] X. Guo, E. Vasco, S. Mi, K. Szot, E. Wachsman, and R. Waser, “Ionic conduction in zirconia films of nanometer thickness,” Acta Mater. **53**(19), 5161–5166 (2005).
[89] D. Pergolesi, E. Fabbri, S.N. Cook, V. Roddatis, E. Traversa, and J.A. Kilner, “Tensile Lattice Distortion Does Not Affect Oxygen Transport in Yttria-Stabilized Zirconia–CeO2 Heterointerfaces,” ACS Nano **6**(12), 10524–10534 (2012).
[90] D.S. Aidhy, and W.J. Weber, “Microstructure design for fast oxygen conduction,” J. Mater. Res. **31**(1), 2–16 (2016).
[91] F. Gunkel, D.V. Christensen, Y.Z. Chen, and N. Pryds, “Oxygen vacancies: The (in)visible friend of oxide electronics,” Appl. Phys. Lett. **116**(12), 120505 (2020).
[92] D.A. Muller, N. Nakagawa, A. Ohtomo, J.L. Grazul, and H.Y. Hwang, “Atomic-scale imaging of nanoengineered oxygen vacancy profiles in SrTiO3,” Nature **430**(7000), 657–661 (2004).
[93] P. Schütz, D.V. Christensen, V. Borisov, F. Pfaff, P. Scheiderer, L. Dudy, M. Zapf, J. Gabel, Y.Z. Chen, N. Pryds, V.A. Rogalev, V.N. Strocov, C. Schlueter, T.-L. Lee, H.O. Jeschke, R. Valentí, M. Sing, and R. Claessen, “Microscopic origin of the mobility enhancement at a spinel/perovskite oxide heterointerface revealed by photoemission spectroscopy,” Phys. Rev. B **96**(16), 161409 (2017).
[94] J.A. Dawson, H. Chen, and I. Tanaka, “Crystal structure, defect chemistry and oxygen ion transport of the ferroelectric perovskite, Na0.5Bi0.5TiO3: insights from first-principles calculations,” J. Mater. Chem. A **3**(32), 16574–16582 (2015).
[95] C. Mitra, T. Meyer, H.N. Lee, and F.A. Reboredo, “Oxygen diffusion pathways in brownmillerite SrCoO2.5: Influence of structure and chemical potential,” J. Chem. Phys. **141**(8), 084710 (2014).
[96] P.P. Dholabhai, S. Anwar, J.B. Adams, P. Crozier, and R. Sharma, “Kinetic lattice Monte Carlo model for oxygen vacancy diffusion in praseodymium doped ceria: Applications to materials design,” J. Solid State Chem. **184**(4), 811–817 (2011).
[97] P. Hatton, and B.P. Uberuaga, “A new compositional microscopic degree of freedom at grain boundaries in complex compounds: a case study in spinel,” Phys. Chem. Chem. Phys. **26**(22), 16125–16138 (2024).